creative commons

COMMONS DEED

저작자표시-비영리-변경금지 2.0 대한민국

이용자는 아래의 조건을 따르는 경우에 한하여 자유롭게

- 이 저작물을 복제, 배포, 전송, 전시, 공연 및 방송할 수 있습니다.

다음과 같은 조건을 따라야 합니다:

저작자표시. 귀하는 원저작자를 표시하여야 합니다.

비영리. 귀하는 이 저작물을 영리 목적으로 이용할 수 없습니다.

변경금지. 귀하는 이 저작물을 개작, 변형 또는 가공할 수 없습니다.

- 귀하는, 이 저작물의 재이용이나 배포의 경우, 이 저작물에 적용된 이용허락조건을 명확하게 나타내어야 합니다.
- 저작권자로부터 별도의 허가를 받으면 이러한 조건들은 적용되지 않습니다.

저작권법에 따른 이용자의 권리는 위의 내용에 의하여 영향을 받지 않습니다.

이것은 이용허락규약(Legal Code)을 이해하기 쉽게 요약한 것입니다.

Disclaimer

dCollection

공학박사 학위논문

Designing Dry Electrode and Solid Electrolyte by Tuning Conductivity for Lithium Batteries

전도도 제어를 통한 리튬 배터리의 건식 전극 및 고체전해질 설계

2023 년 8 월

서울대학교 대학원

화학생물공학부

김 현 태

Designing Dry Electrode and Solid Electrolyte by Tuning Conductivity for Lithium Batteries

전도도 제어를 통한 리튬 배터리의 건식 전극 및 고체전해질 설계

지도 교수 최 장 욱

이 논문을 공학박사 학위논문으로 제출함

2023 년 8 월

서울대학교 대학원

화학생물공학부

김 현 태

김현태의 공학박사 학위논문을 인준함

2023 년 8 월

위 원 장 _____ 성 영 은 _____ (인)

부위원장 _____ 최 장 욱 _____ (인)

위 원 _____ 이 규 태 _____ (인)

위 원 _____ 김 기 재 _____ (인)

위 원 _____ 문 준 영 _____ (인)

Abstract

Designing Dry Electrode and Solid Electrolyte by Tuning Conductivity for Lithium Batteries

Hyuntae Kim

School of Chemical & Biological Engineering

The Graduate School

Seoul National University

Lithium-ion batteries have become an important component in many electronic devices, from smartphones to electric vehicles. With the development of medium and large batteries, one of the main challenges for implementing batteries with higher energy density is to achieve efficient charge transfer within the batteries. Ion conductivity in an electrolyte and electrical conductivity in an electrode are key factors that determine the rate at which charges can pass through a battery and are crucial to the performance of the low conductivity can lead to reduced energy efficiency, reduced battery life, and reduced power output. Many researchers have explored various technologies such as developing new materials with high conductivity, optimizing battery design to minimize the distance of ion transport, and

improving manufacturing processes to reduce impurities. This study proposes the importance of conductivity tuning for process improvement in dry electrode and oxide solid electrolytes.

The first chapter introduces the importance of conductivity tuning with a brief theoretical background. The second chapter demonstrates that the electrochemical performance of high-loading (above 30 mg/cm^2) dry-processed cathodes using high-nickel cathode active material (NCM811) can be further improved when ozonated CNTs are employed as the conductive agent. In the third chapter, a method for manufacturing a solid electrolyte membrane with exceptional physical properties and electrochemical performance is presented. This is achieved by improving ionic conductivity through the addition of PVdF, one of the highest dielectric constant materials, to an organic/inorganic hybrid solid electrolyte based on in-situ crosslinking. Finally, the fourth chapter summarizes key findings from previous chapters.

In summary, this dissertation aims to provide various methods to improve conductivity when developing a new battery element process for implementing high-energy density batteries, which will provide important insights into the development of next-generation batteries.

Keywords: Conductivity, Dry-processed cathodes, Ozonation, Carbon nanotubes, Hybrid solid electrolyte, Crystallinity

Student Number: 2018-34787

Contents

List of Tables

List of Figures

Chapter 1. Introduction

1.1. Conductivity Issues in Battery Society

Since Sony launched the first commercial lithium-ion battery in 1991, the lightweight and low reduction potential of lithium metal (- 3.04 V vs. standard hydrogen electrode) have made it widely used in small portable energy storage devices and larger devices such as hybrid and electric vehicles. As these storage devices increase in size, the market is looking for batteries with higher energy density, which requires the use of materials with improved conductivity.[1]

In operating electrochemical cells **(Figure 1.1)**, the critical phenomena involve the transportation of conducting ions and electrons between the cathode and anode. Generally, electrochemical reactions refer to oxidation and reduction reactions in which electrons are involved, and as a large number of electrons move smoothly between the anode and cathode without hindrance, the magnitude of the driving force of the battery increases.[2] From thermodynamical point of view, **Equation (1.1)** below expresses the relationship between the resistance of a battery and the difference between its operating voltage and standard voltage. Put simply, the smaller the battery's resistance, the closer the two voltages will be.[3, 4]

$$E = E_0 - [(\eta_a)_{an} + (\eta_a)_{cat}] - [(\eta_c)_{an} + (\eta_c)_{cat}] - iR_i = iR \qquad (1.1)$$

(E_0 = standard cell potential, $(\eta_a)_{an}$, $(\eta_a)_{cat}$ = activation polarization at the anode and cathode, $(\eta_c)_{an}$, $(\eta_c)_{cat}$ = concentration polarization at the anode and

cathode, R_i = internal resistance (ohmic polarization) of the cell, R = apparent cell resistance)

All these three terms are deeply related to conductivity: (1) activation polarization occurs when the rate of the charge transfer reaction between the electrode and the electrolyte interface is limited by the kinetics; (2) concentration polarization occurs due to the mass transport limitations; (3) internal resistance of the cell (ohmic polarization) is linked to the resistance of individual components within a cell as well as the resistance that arises from contact issues among them **(Table 1.1)**.[5, 6] The above theory highlights that to experimentally enhance battery performance, it is crucial not only to improve the material's conductivity but also to reduce the resistance at the interface between battery components.

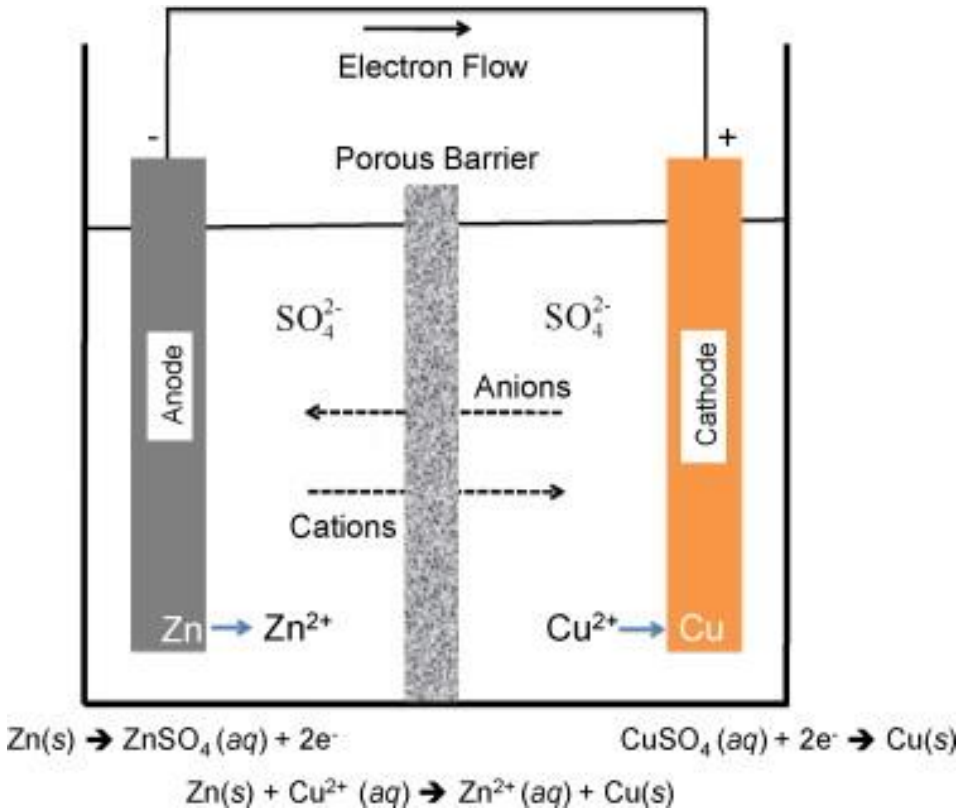

Figure 1.1 A typical illustration of the electrochemical cell.[7] Copyright 2010, Elsevier.

Table 1.1 Type of internal resistance of the electrochemical cell.[3]

Type of resistance	Internal resistance of the electrochemical cell
Ionic	- Electrode particle - Electrolyte
Electrical	- Electrode particle - Conductive additives - Percolation network of additives in electrode - Current collectors - Electrical taps
Interfacial	- Between electrolyte and electrodes - Between electrode particles and conductive additives - Between electrode and current collector - Between conductive additives and current collector

1.2. References

[1] J. M. Tarascon, M. Armand, *Nature* **2001**, *414*, 359.

[2] M. Winter and R. J. Brodd, *Chem. Rev.* **2004**, *104*, 4245-4270.

[3] D. Linden (2002). *Handbook of batteries (3rd edition)*. McGraw-Hill

[4] Gaskell, D. R., & Laughlin, D. E. (2017). *Introduction to the Thermodynamics of Materials.* CRC press.

[5] C. Delacourt, L. Laffont, R. Bouchet, C. Wurm, J. B. Leriche, M. Morcrette, J. M. Tarascon and C. Masquelier, *J. Electrochem. Soc.* **2005**, *152*, A913.

[6] M. Kaneko, M. Nakayama, Y. Wakizaka, K. Kanamura and M. Wakihara, *Electrochim. Acta* **2008**, *53*, 8196-8202.

[7] M. Park, X. Zhang, M. Chung, G. B. Less and A. M. Sastry, *J. Power Sources* **2010**, *195*, 7904-7929.

Chapter 2. Ozone-Treated Carbon Nanotube as a Conductive Agent for Dry-Processed Lithium-Ion Battery Cathode

2.1. Introduction

The demand for cost-effective, eco-friendly, and high-energy-density lithium-ion batteries (LIBs) has surged due to the recent growth of the electric vehicle sector.[1, 2, 3, 4] Many battery manufacturers have begun on a substantial endeavor to modify their entire production process to meet the escalating environmental and performance requirements, while simultaneously reducing manufacturing costs.[5, 6, 7, 8, 9] Conventional wet-process electrode manufacturing uses toxic, high-boiling-point solvents like N-methyl-2-pyrrolidone (NMP) for electrode slurry preparation, necessitating significant heat energy for solvent drying.[10, 11] This drying process can also cause uneven dispersion of binder materials like polyvinylidene fluoride (PVDF), especially at high loading levels, adversely impacting battery performance.[12, 13]

The dry electrode process has attracted significant attention from researchers for its potential to reduce production costs, simplify manufacturing schemes, and mitigate process-related non-uniformity in the electrode composition by eliminating the requirement for the solvent drying process. This approach consists of physically mixing active electrode materials (e.g., lithium nickel-cobalt-manganese oxide (NCM)) with conductive agent and binder without solvent, followed by roll-pressing

and calendering the resultant electrode composite on the current collector.[14, 15] By eliminating solvent drying, this technique can significantly improve the electrode density, simplify high-loading electrode production, and reduce costs by reducing heat energy consumption. The remarkable potential of this technology was underscored by the acquisition of Maxwell Technologies by Tesla Inc. in 2019.[16]

Despite its considerable potential, the dry electrode process presents multiple technical obstacles, including insufficient dispersion of conductive materials due to the lack of solvent, which is particularly pronounced when employing conventional conductive agents with point-like morphologies, such as carbon black (CB). While CB has been frequently used in cathode fabrication due to its availability and acceptable electrical conductivity, its incorporation into the cathode composite through physical mixing without solvent often results in the agglomeration, poor filling, and dead ends, impeding charge transfer and causing poor electrical conduction.[17, 18, 19]

Carbon nanotubes (CNTs) offer a promising solution owing to their high aspect ratio and exceptional electrical conductivity.[20, 21] Compared to the point-to-point contacts that characterize CB particles, long CNT strands can facilitate superior charge transfer pathways based on their linear morphologies.[22, 23, 24] For optimal performance, CNTs should be dispersed uniformly throughout the dry cathode composite, thereby producing effective ion and charge transfer networks. However, their tendency to aggregate limits dispersion and active material contact when mixed without solvent, especially at high electrode loading levels.[25, 26, 27] Surface functionalization of CNTs with various strong liquid-phase oxidants[28, 29, 30, 31] can introduce oxygen-based functional groups, such as carboxylic acid, hydroxyl, and carbonyl groups, to the surface of CNTs. This modification reduces their tendency

to aggregate[32, 33] while increasing their affinity for active materials, leading to improved electrochemical reaction kinetics of the given dry-processed LIB electrode even with low amounts of conductive agents.[34] The use of liquid-phase strong acidic oxidizers, such as mixed acid,[29, 30] can effectively introduce functional groups to the CNT surfaces; however, they can also severely damage the sp^2 system of nanotubes, resulting in decreased electrical conductivity, which calls for optimization based on trials and errors and extra drying processes.

Instead, utilizing gas-phase oxidants such as ozone (O_3) eliminates the requirement for additional drying processes and simplifies optimization. Furthermore, it is environmentally friendly since excess ozone can be decomposed into oxygen (O_2) through thermal treatment above 200 °C without producing any waste chemicals. In this communication, we present the fully solventless dry cathode manufacturing process involving ozonated single-walled CNTs (O-SWCNTs) as the conductive agent. Under optimized cathode composite preparation conditions, high-nickel cathode active material ($LiNi_{0.8}Co_{0.1}Mn_{0.1}O_2$ (NCM811)) was physically mixed with conductive agents and polytetrafluoroethylene (PTFE) binder in a 96:2:2 weight ratio and lithium half-cells were prepared using the calendered composite as the cathode. The electrochemical performance of the cell utilizing O-SWCNT as the conductive agent was superior to those utilizing conventional CB (Super P®, denoted as SP) and pristine SWCNT **(denoted as just SWCNT, Table 2.1)**. This was attributed to the increased affinity of the conductive agent to the active material and the protective role of O-SWCNT for the cathode interface against uncontrolled side reactions, which keeps the electrode resistance stable during cycling. The present study underscores the possible significance of CNTs in electrode production through dry processing methods.

2.2. Experimental Methods

Ozonation of SWCNTs: SWCNTs (Tuball^{TM}, OCSiAl group) underwent ozone treatment using a homemade ozone treatment setup. An O_3/O_2 gas mixture, generated by passing pure O_2 through a commercial ozone generator (LAB-S, Ozonetech), was introduced into a glass tube. The concentration of O_3 in O_2 was regulated by adjusting the UV intensity and the O_2 flow rate. The as-received SWCNTs were placed in the glass tube reactor and exposed to the O_3/O_2 gas mixture. Optimized ozone treatment conditions were applied to SWCNT ozonation.

Preparation of the cathodes and electrochemical cells: The dry-processed cathodes were fabricated by initially mixing NCM811 (D_{50} = 10 μm), conductive agents (Super-P, SWCNT, O-SWCNT), and polytetrafluoroethylene (PTFE) powder as a binder using a planetary centrifugal mixer (AR-100, THINKY, Japan) in a weight ratio of 96:2:2. Super-P (Imerys Graphite & Carbon, Switzerland) was employed as the reference conductive agent. The mixed powders were calendered into sheets with a 3-roll-mill at 60°C, and subsequently adhered to 15 μm-thick Al foil (Wellcos, South Korea) by roll pressing at 80°C. The electrode density after these processes ranged from 3.2 to 3.4 g/cm^3 and the mass loadings of cathodes corresponded approximately to 30 mg/cm^2 and 40 mg/cm^2, respectively. The NCM811 active material and PTFE binder were supplied by Hyundai Motor Company. CR2032 coin-type lithium half-cells were assembled in an Ar-filled glove box. A 150 μm-thick lithium foil (Honjo Metal, Japan) was used as a reference and counter electrode. A PE separator (SK Innovation, South Korea) and 1 M $LiPF_6$ in

EC/DEC (1/1 = v/v) with 10 wt% FEC (Soulbrain, South Korea) were used as a separator and an electrolyte, respectively.

Characterization of Materials: The chemical bonds and defects of the SWCNTs were analyzed using Raman spectroscopy (DXR2xi, Thermo Fisher Scientific, USA). The electrical conductivity of cathodes was measured using chronoamperometry with a potentiostat (VSP, Bio-logic, France). The tensile strength of the cathodes was examined with a universal testing machine (UTM) (QM100S, QMESYS, South Korea), following the ASTM D638 standard test method. The cross-sections of the cathodes were prepared using a cross-section polisher (IB-19530CP, JEOL, Japan). The surface and cross-sectional images of the cathodes were acquired using field emission-scanning electron microscopy (FE-SEM) (JSM-7800F Prime, JEOL, Japan). The dispersibility of the electrode was investigated by a 2D mapping technique using confocal Raman microscopy (inViaTM, Renishaw, UK). The porosity and 3D distributions of the cathodes were assessed with a system combining high-resolution 3D X-ray microscopy (XRM, spatial resolution = 0.5 μm) with computed tomography (Xradia 620 Versa, Carl Zeiss, USA). The surface components of cathodes and oxygen components of O-SWCNT were identified using X-ray photoelectron spectroscopy (XPS) (Axis-Supra, Kratos, UK). The surface energy of SWCNTs was evaluated by contact angle measurement (SmartDrop, Femtobiomed, South Korea).

Electrochemical Characterization: All electrochemical cells were rested at room temperature for 20 h to ensure that the cathodes were sufficiently soaked with the electrolyte prior to electrochemical tests. Each cycle was conducted in

galvanostatic charge/discharge mode within the potential range of 2.5–4.25 V (vs Li/Li+) at 25°C. The CC/CV and CC modes were adopted for the charge and discharge processes, respectively, using a battery cycler (WBCS3000L, WonAtech, South Korea). Before cycling, the formation process was performed for one cycle at 0.1C with a cut-off condition of 0.05C. Cyclability tests were performed at 0.33C with a cut-off condition of 0.165C, following the aforementioned formation process. Rate capability tests were carried out by applying various C-rates from 0.1C to 1C. Electrochemical impedance spectroscopy (EIS) analysis with AC current was performed over a frequency range of 0.01 Hz–1 MHz at 25°C with a voltage perturbation of 10 mV using a potentiostat (VSP, Bio-logic, France). The resulting Nyquist plots were fitted to the equivalent circuit using the EC-Lab® software.

2.3. Results and Discussion

Liquid-phase surface functionalization of SWCNT using mixed acid typically results in sturdy buckypapers **(Figure 2.1)**, which is not applicable for the physical mixing of the dry electrode process. A 3:1 volumetric mixture of concentrated H_2SO_4 (99%, Daejung, Korea)-HNO_3 (70%, Daejung, Korea) was used as an oxidizing agent for as-received SWCNTs. A 150 mg sample of SWCNT was mixed with 48 mL of oxidant and was acid-treated at 60 °C for 3 hours. Upon filtering and drying the oxidized SWCNT dispersion, a buckypaper of SWCNT was formed due to the agglomeration of SWCNTs resulting from increased hydrophilicity. The buckypaper was not applicable for dry fabrication process with NCM811 due to poor interfacial contact with the NCM particles. Using ozone as the oxidant, SWCNT can maintain its initial fluffy powdery texture, making it easily mixed with cathode active materials and binder. Optimal ozone treatment **(Table 2.2, 8 μg O_3/cc O_2)** was adopted for 15 minutes using a custom-made flow-type ozone generator **(Figure 2.2a)** at room temperature. The treatment duration was determined based on electrochemical performance of cathodes **(Figure 2.3)**. As a result of the ozone treatment, oxygen-containing groups, such as hydroxyl, carbonyl, and carboxylic acid, were introduced as indicated by the C 1s X-ray photoelectron spectroscopy (XPS) and the CHNO combustion elemental analysis results shown in **Figures 2.4a–c**. The increased hydrophilicity observed suggests a increase in the surface energy of the SWCNT conductive agent as shown in **Figure 2.4d**.

Furthermore, the Raman spectra also showed an increase in the intensity of the D band of the sp^2 hybridized system, which reflects the presence of surface

functional groups **(Figure 2.5)**. The D-band and the G-band in the Raman spectra of SWCNTs appeared at 1338 cm^{-1} and 1588 cm^{-1}, respectively.[35] The C-C bond stretching in the graphitic carbon lattice of SWCNTs gives rise to the G-band peaks in Raman spectra. The D-band peaks originate from the disorder in sp^2 hybridized carbon network. Therefore, the amount of defects in SWCNTs can be analyzed by the ratio of the intensities of the D-band and G-band (I_D/I_G ratio). The increase in I_D/I_G ratio of SWCNTs after the ozone treatment was confirmed, supporting the functionalization of the SWCNT surface by ozonation. The Raman spectra of 10 spots of each sample were collected and averaged for the calculation of I_D/I_G ratio. We used O-SWCNTs to fabricate cathodes through the following dry cathode process: 1) mixing NCM811 active materials, conductive agents, and PTFE binders, 2) fibrillating PTFE, 3) calendering the composite, and 4) adhering the electrode to the Al current collectors, as illustrated in **Figure 2.2b**. The detailed procedures are described in the Section 2.2. We prepared the reference cathodes in parallel, where SP and pristine SWCNT were used as conductive agents for comparison. The scanning electron microscopy (SEM) images **(Figure 2.6)** revealed that the SP cathode was not well-filled with conductive material, and some parts were aggregated compared to the other SWCNT cathodes, despite the high shear force of the calendering process. In the SWCNT cathodes, most of the empty spaces in the cathode were well-filled, which is expected to improve the electrical conductivity of the cathode.

Figure 2.1 The formation of SWCNT buckypaper after acid treatment.

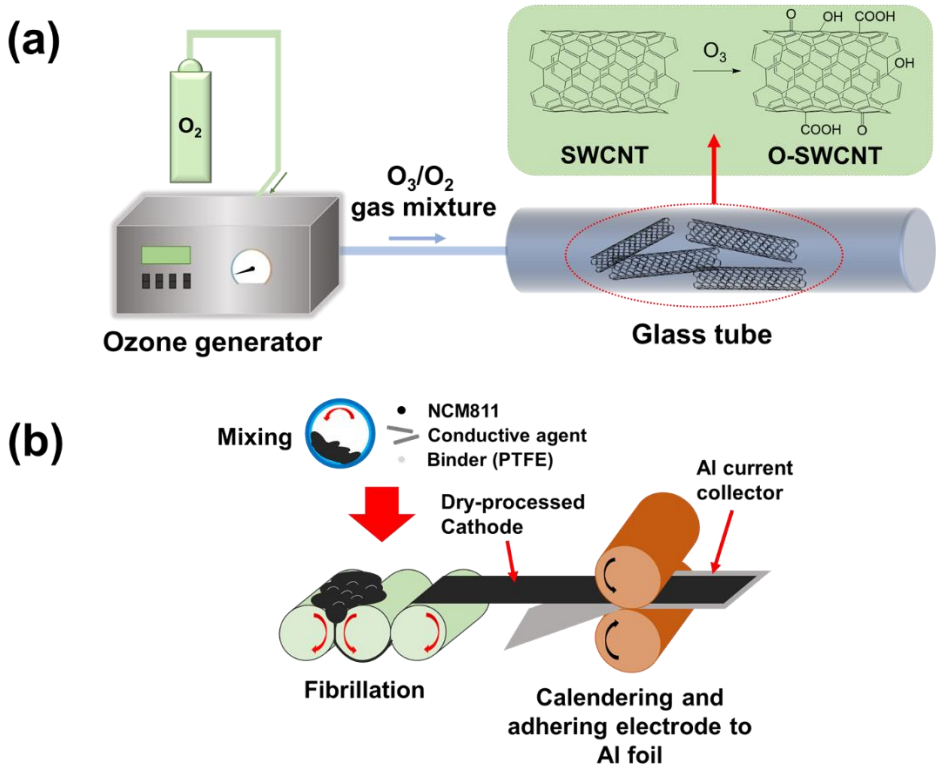

Figure 2.2 The ozonation of SWCNT and its application to the dry cathode process. (a) Schematic illustration of SWCNT ozonation. (b) Schematic illustration of dry cathode preparation.

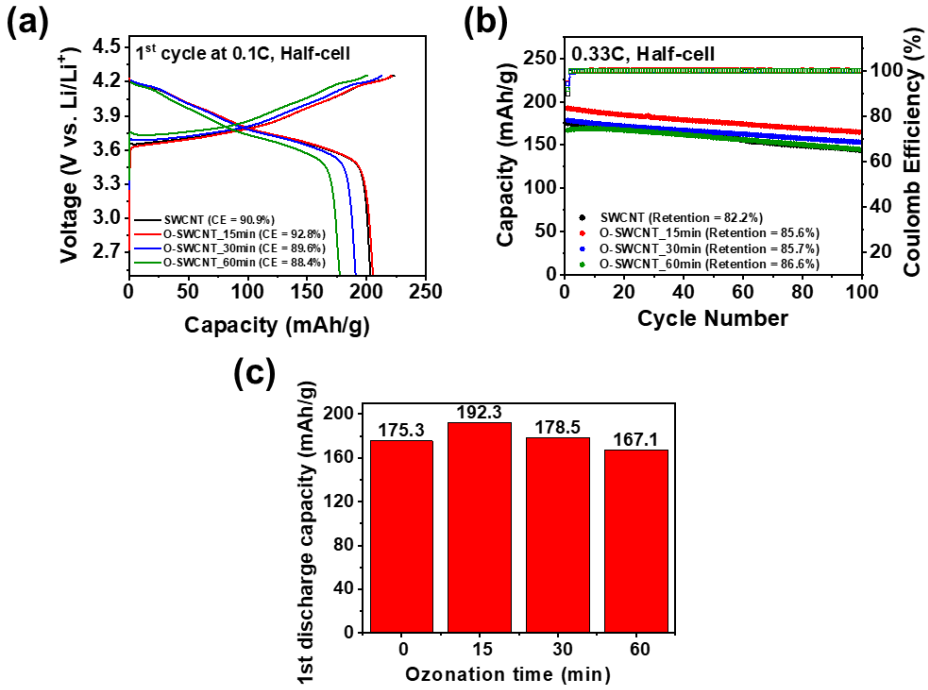

Figure 2.3 Electrochemical performance of O-SWCNT cathodes with respect to the ozonation time (1C = 200 mA/g). (a) Voltage profiles of cathodes in their first formation cycle at 0.1C. (b) Cycling tests and CE trends of cathodes measured at 0.33C. (c) The trend of the first discharge capacity as a function of the ozonation time.

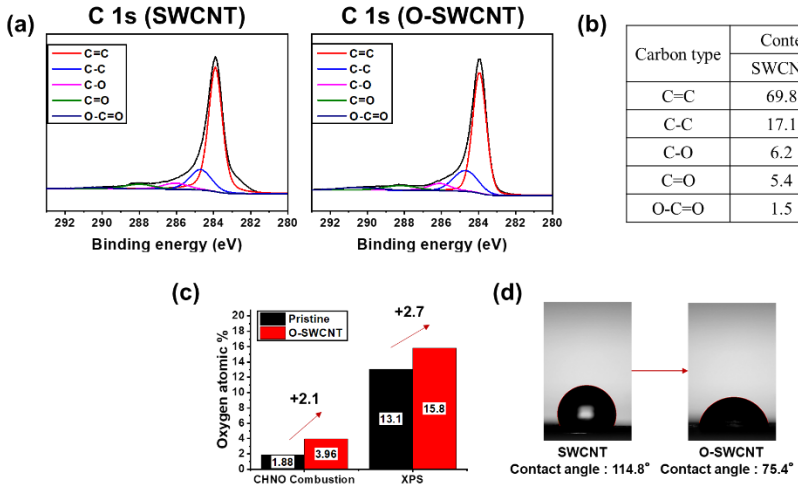

Carbon type	Contents (atomic %)	
	SWCNT	O-SWCNT
C=C	69.8	65.3
C-C	17.1	18.9
C-O	6.2	7.0
C=O	5.4	5.5
O-C=O	1.5	3.4

Figure 2.4 Characterization of SWCNT. (a) C 1s XPS spectra of SWCNT (left) and O-SWCNT (right) samples. (b) Deconvolution results of the C 1s XPS spectra of SWCNT and O-SWCNT. (c) C/O Elemental analysis results based on the CHNO combustion analysis and the XPS. (d) Contact angle measurement results.

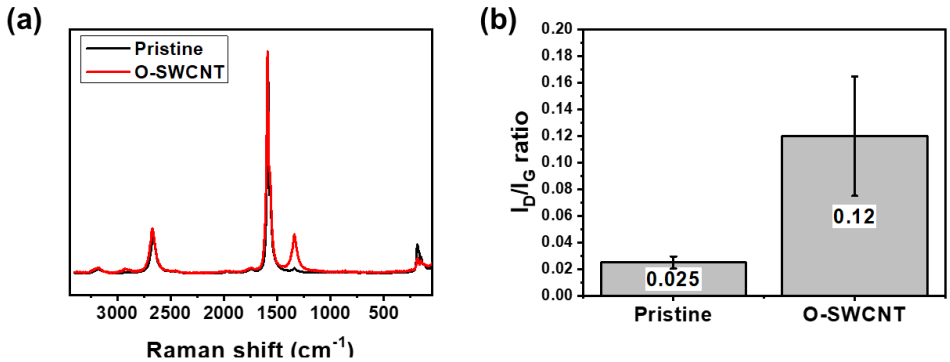

Figure 2.5 (a) Intensity-normalized Raman spectra and (b) I_D/I_G ratio of SWCNT samples.

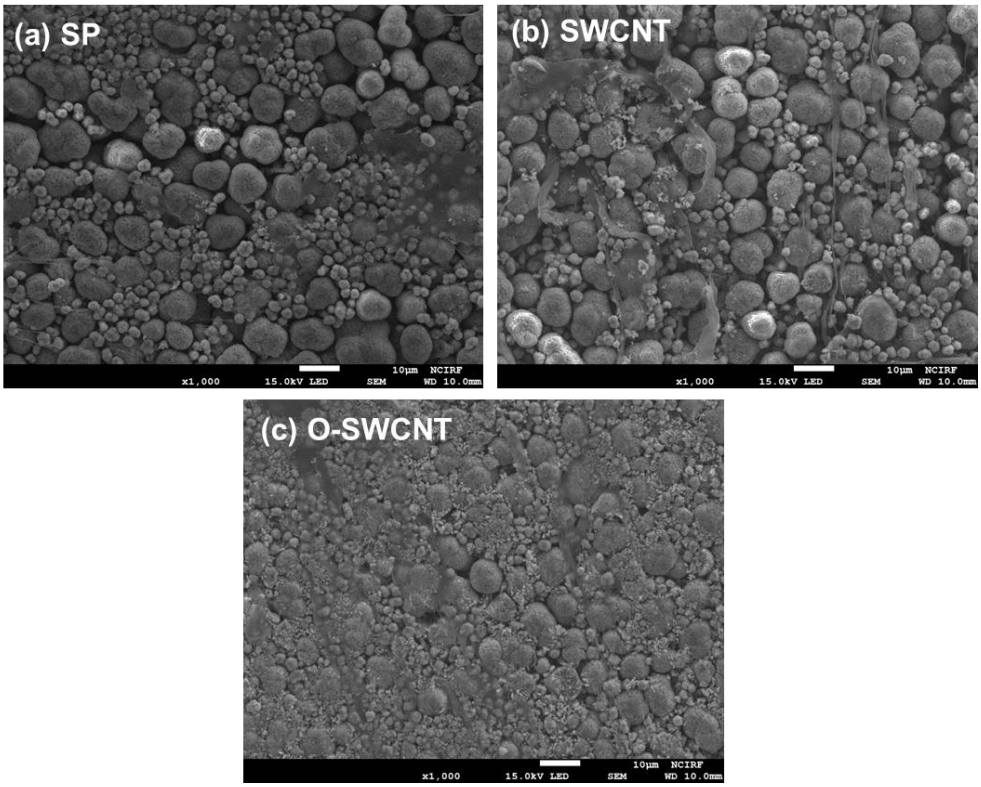

Figure 2.6 Top-view SEM images of the (a) SP, (b) SWCNT, (c) O-SWCNT cathodes.

Table 2.1 Properties of pristine SWCNT.

Sample name	**Diameter [nm]**	**Surface area [m^2/g]**	**Length [μm]**	**Purity [wt%]**
SWCNT	1.6±0.4	800-1600	5	99

Table 2.2 Parameters of SWCNT ozonation.

Sample name	**Temperature**	**Ozone concentration**	**Ozone flow rate**	**Time**
O-SWCNT	25 °C	8 μg O_3/cc O_2	1 L/min	15 min

To assess the quality of binding among elements in the cathode, we used a high-resolution 3D X-ray microscope (XRM) to examine the porosity of the cathode (*i.e.*, the fraction of voids) to determine whether the binding of the conductive agent inside the cathode had been improved **(Table 2.3)**. This technique is combined with microcomputed tomography (micro-CT) to provide a 3D image of a sample by reconstructing a series of 2D X-ray projection images (XY, YZ, ZX planes) while rotating the sample,[36] as displayed in **Figure 2.7**. Porosity is calculated based on the amount of electrode material detected within the spatial resolution of XRM. The SWCNT cathodes showed better filling than the SP cathode, indicating that the application of SWCNTs in the dry electrode process has the potential to reduce voids within the resultant electrode. The porosity of O-SWCNT was even lower than that of SWCNT, presumably due to the surface treatment that increased the density of the cathode. This affinity of the two SWCNT cathodes was also demonstrated when the tensile strength was measured **(Figure 2.8)**. The ozonation of SWCNT resulted in a twofold increase in the tensile strength of the dry-processed electrode. After calendering, the calculated porosities of SP, SWCNT, and O-SWCNT cathodes changed from 28.12% to 20.90%, 17.42% to 16.57%, and 15.68% to 13.89%, respectively. The two SWCNT cathodes are considered to have smaller changes in porosity after calendering due to the denser cathode structure because the SWCNTs already effectively filled voids before calendering. Despite the potentially adverse effects on ionic transport caused by the low porosity of high-loading SWCNT-based cathodes, we think that the enhanced electrical conductivity and interphase properties outweighed these effects, leading to the high rate performance (*vide infra*).

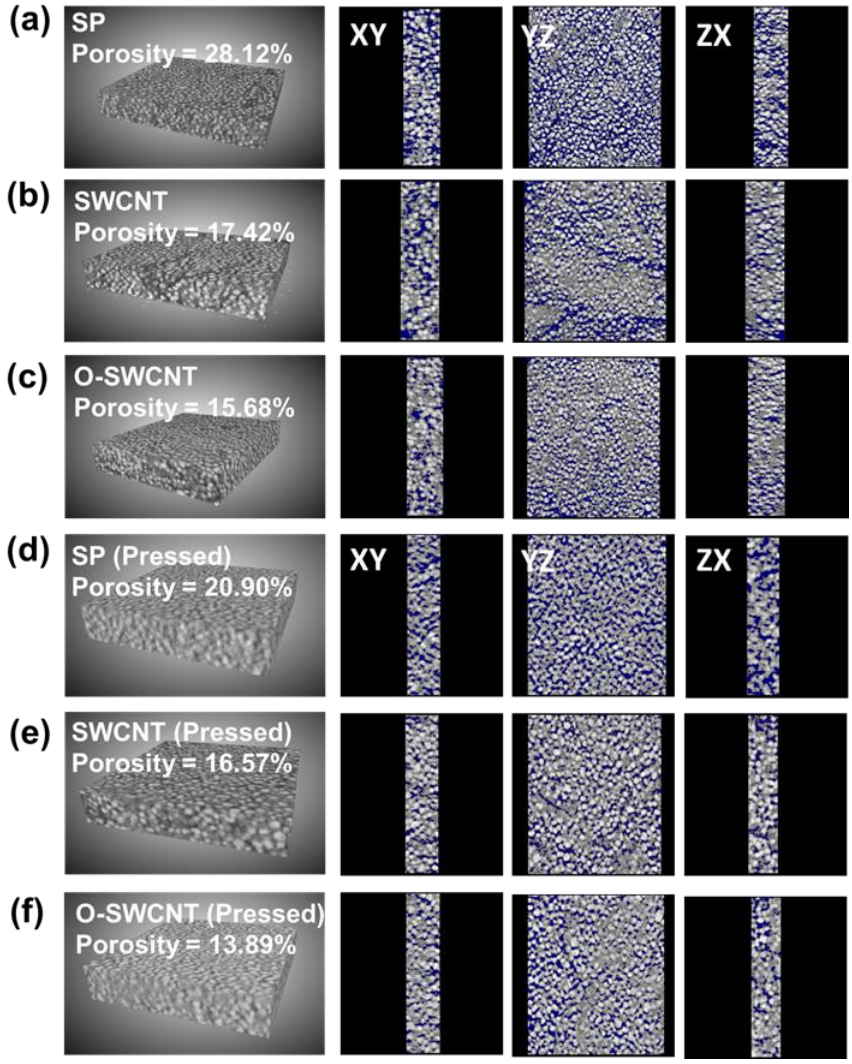

Figure 2.7 3D reconstructed XRM images (spatial resolution: 0.5 μm) of SP, SWCNT, O-SWCNT cathodes (a, b, c) before and (d, e, f) after calendering. The dimension of 3D images is 60 μm x 270 μm x 300 μm. 2D XRM images of each cathode are also included alongside the XY, YZ, ZX plane.

Table 2.3 Porosity information from XRM analysis in Figure 2.7.

Sample	Total volume of tomography [μm³]	Pore volume of tomography [μm³]	Porosity [%]
SP (Before calendering)	5,091,569.63	1,431,749.38	28.12
SP (After calendering)	2,617,043.30	546,962.05	20.90
SWCNT (Before calendering)	5,099,506.88	888,334.10	17.42
SWCNT (After calendering)	2,596,919.87	430,309.62	16.57
O-SWCNT (Before calendering)	5,002,412.95	784,378.35	15.68
O-SWCNT (After calendering)	2,663,991.13	370,028.37	13.89

(a)

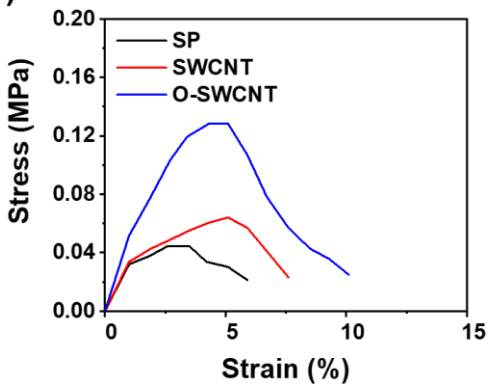

(b)

	Tensile stress (gf/mm^2)
SP	5.09
SWCNT	6.73
O-SWCNT	13.09

Figure 2.8 (a) Stress-strain curves of the SP, SWCNT, O-SWCNT cathodes. (b) Calculated tensile strength results.

We evaluated the electrochemical performance of all dry-processed cathodes at a high loading level of 30 mg/cm^2 by assembling CR2032 type coin half-cells, with the working electrode as the cathode and lithium metal as the anode. The voltage profiles of all cathodes in their first cycle did not exhibit different shapes, implying that the different conductive agents had a negligible impact on the intrinsic reaction chemistry of NCM811 in storing Li ions. Nonetheless, the initial Coulombic efficiencies (CE) of the SP, SWCNT, and O-SWCNT cathodes were different to be 90.5%, 90.9% and 92.8%, respectively **(Figure 2.9a)**. In comparison to the SWCNT-based cathodes, the SP cathode had a higher overpotential during the first charge cycle. Cycling performance tests of all cathodes were also evaluated in the voltage range of 2.5−4.25 V at 0.33C. **(Figure 2.9b)** The O-SWCNT cathode exhibited a significantly higher initial specific discharge capacity (192.3 mAh/g) than the SWCNT cathode (175.3 mAh/g) and SP cathode (130.6 mAh/g). From the cycling stability viewpoint, the O-SWCNT cathode retained 85.6% of its initial capacity after 100 cycles, while the SWCNT and SP cathodes retained 82.2% and 57.0%, respectively, after the same number of cycles. Also, the O-SWCNT cathode showed the most advanced performance at all rates in the rate capability test **(Figure 2.9c)**. The remarkable electrochemical performance of the dry-processed O-SWCNT cathode can be attributed to the optimized contact established between O-SWCNT and NCM811 particles, along with the optimized functionalization process employed **(Figure 2.3, 2.10)**.[37] In the same context, the stability of the cathode-electrolyte interphase (CEI) layer is likely the main origin of the distinct performance among the three conductive agents-based cathodes; the presence of oxygen functional groups in the O-SWCNT cathode leads to more complete coverage of the conductive agent over NCM811 particles and protects them from undesired side reactions during

cycling.[38, 39] This protective function of O-SWCNT keeps the interfacial resistance more stable (detailed analysis in the next paragraph) to achieve the higher specific capacity and the improved cyclability of the O-SWCNT cathode. We believe that the performance of the electrodes at high C-rates (*i.e.*, 1C) is suboptimal, possibly due to insufficient dispersion of conductive agents affected by an instrument and other conditions in the dry-mixing process. This rationale was reflected in the 2D Raman mapping of the electrodes displayed in **Figure 2.11**. It can be seen that two distinctive carbon peaks, the D band (~1350 cm^{-1}) and the G band (~1580 cm^{-1})[35], were clearly detected in the electrodes except for the SP electrode. This indicates that the SP in the electrode was not uniformly distributed, which was also confirmed by the SEM image in **Figure 2.6**. In case of the two SWCNT-based electrodes, however, it was difficult to determine whether the dispersion within the electrode composite was uniform. Due to the strong affinity between the SWCNTs, many aggregation points were still present in the electrode even after the cathode was fabricated, and the O-SWCNT electrode exhibited the similar dispersion behavior. It is noteworthy that the excellent electrical conductivity of CNTs compensates for the suboptimal dispersibility of dry electrodes. Improving the dispersion of carbon-based conductive agents would further improve the performance, which is a possibility that merits further investigation. Increasing the loading level to 40 mg/cm^2 also resulted in the same trend **(Figure 2.12, Table 2.4)**, with the O-SWCNT dry-processed cathode showing superior performance compared to the SWCNT and SP cathodes. The reduced discrepancy in performance among the cathodes with a thickness of 40 mg/cm^2 can be ascribed to the attenuated shear effect resulting from the augmented thickness of the cathode.

The disparity between the 100-cycled performances of the dry-processed

electrodes containing SP and SWCNT conductive agents was elucidated by the significant difference in their respective resistances in CEI layers (R_{CEI}) according to the electrochemical impedance spectroscopy (EIS) analysis. Impedance spectra obtained prior to and after 100 cycles of charge and discharge are presented in **Figures 2.9d and 2.9e**. Prior to the cycles, the charge-transfer resistance (R_{ct}) of the SP-based electrode was notably higher (202 Ω) than those of the SWCNT-based (R_{ct} = 67 Ω) and O-SWCNT-based (R_{ct} = 43 Ω) electrodes. This difference may be attributed to variations in the effectiveness of carbon-NCM811 contact. Following 100 cycles, two distinct semicircles were clearly observed in the EIS spectra of the SWCNT-based dry-processed electrodes, representing R_{CEI} (left) and R_{ct} (right), respectively.[40, 41, 42] In contrast, the SP-based electrode did not display clear distinction

between R_{CEI} and R_{ct}, but showed a large, merged semicircle of an overall value (R_{ct} + R_{CEI}) of 166 Ω. The R_{CEI} values for the SWCNT-based (R_{CEI} = 14 Ω, R_{ct} = 17 Ω) and O-SWCNT-based (R_{CEI} = 11 Ω, R_{ct} = 15 Ω) electrodes were notably lower compared to the SP-based cathode. These results once again suggest that the inferior cycling and rate performance of the SP-based dry-processed cathode is closely linked to its CEI characteristics.

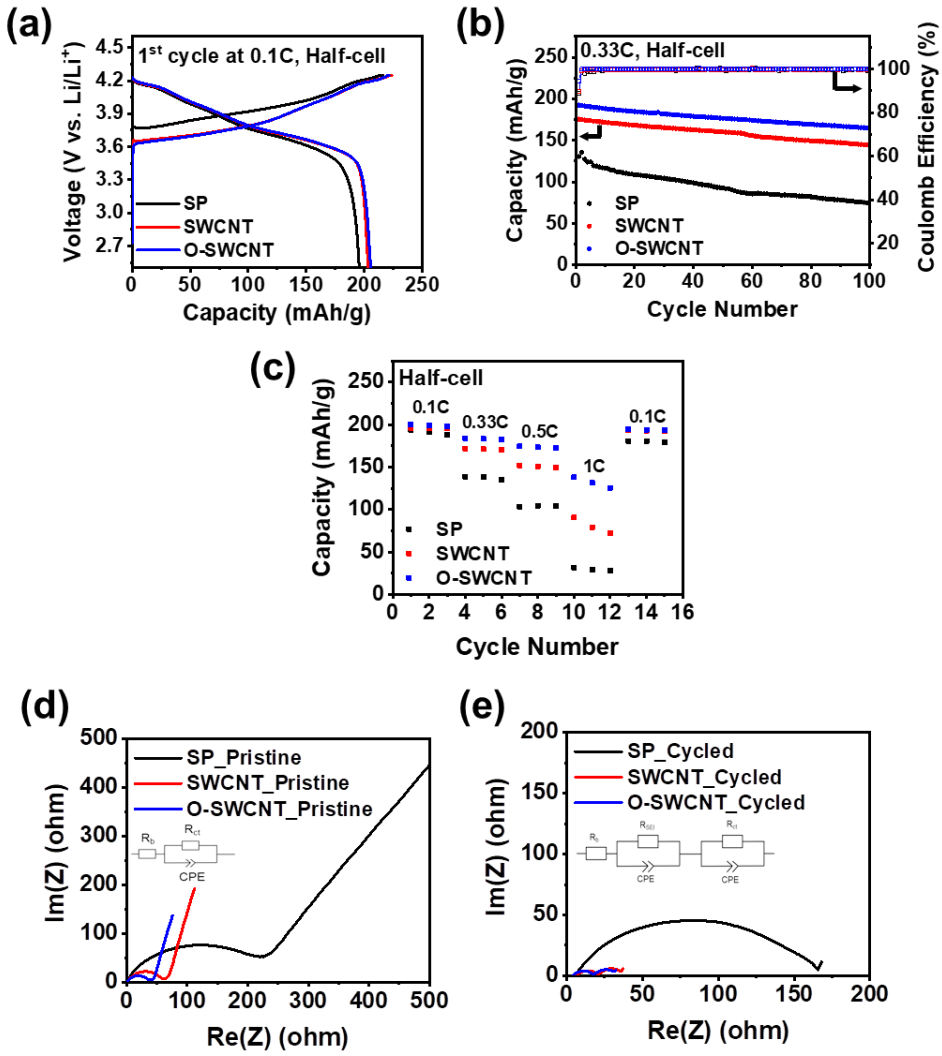

Figure 2.9 Electrochemical performance of all cathodes at the loading level of 30 mg/cm^2 at room temperature in half-cell configurations (1C = 200 mA/g). (a) Voltage profiles of cathodes in their first formation cycle at 0.1C. (b) Cycling tests and CE trends of cathodes measured at 0.33C. (c) Rate capability test measured at various C-rates. All electrochemical tests were carried out after one formation cycle at 0.1C in the voltage window of 2.5−4.25 V. EIS plots of all cathodes (d) before cycling and (e) after 100 cycles.

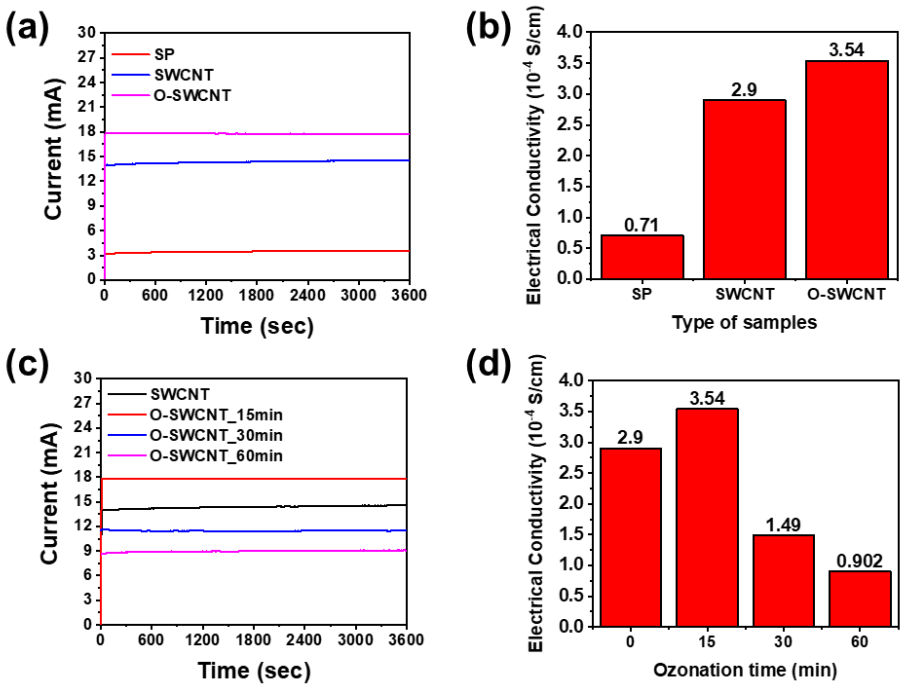

Figure 2.10 Electrical conductivity experiments using chronoamperometry with the constant voltage of 0.5 V in 1 hr. (a) Electric current trend of SP, SWCNT, O-SWCNT cathodes. (b) Calculated electrical conductivity of SP, SWCNT, O-SWCNT cathodes. (c) Electric current trend of cathode samples with different ozonation times. (d) Calculated electrical conductivity of cathode samples with different ozonation times.

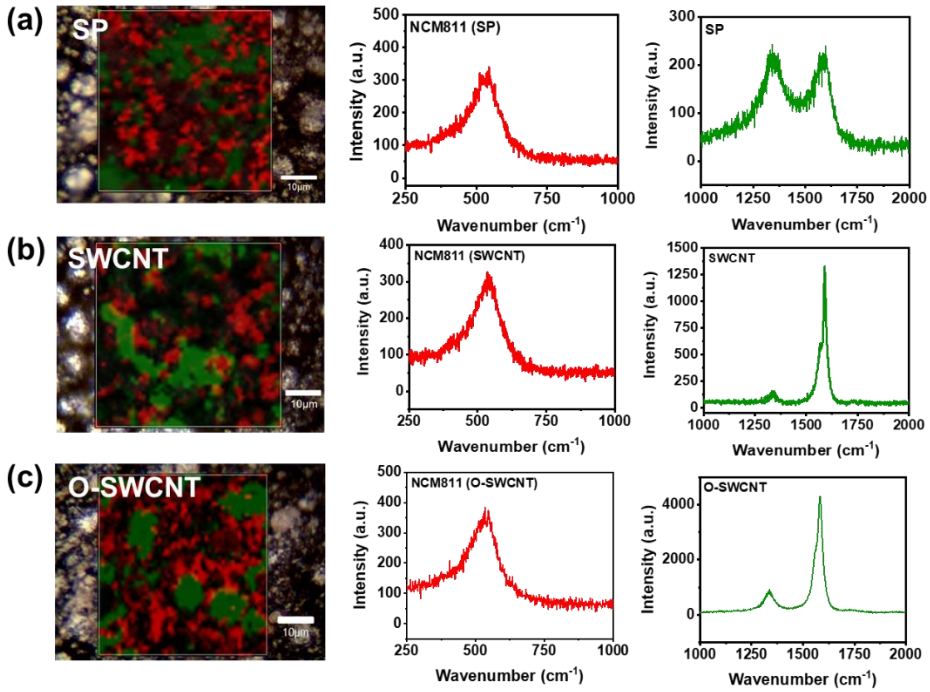

Figure 2.11 2D Raman mapping images of the (a) SP, (b) SWCNT, (c) O-SWCNT cathodes covering the area of 50 μm × 50 μm. Each electrode consists of NCM811 active materials (shown in red) and conductive agents (shown in green).

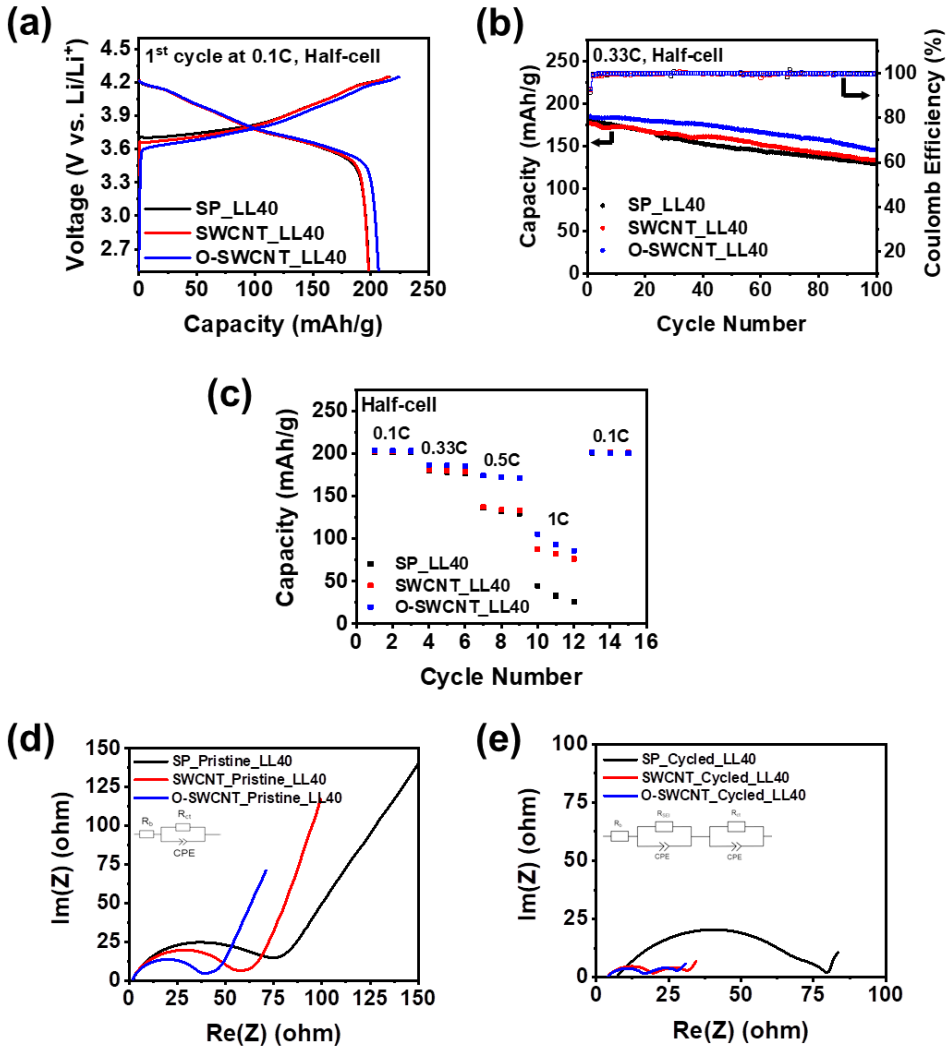

Figure 2.12 Electrochemical performance of all cathodes at the loading level of 40 mg/cm^2 at room temperature in half-cell figurations (1C = 200 mA/g). (a) Voltage profiles of cathodes in their first formation cycle at 0.1C. (b) Cycling tests and CE trends of cathodes measured at 0.33C. (c) Rate capability test measured at various C-rates. All electrochemical tests were carried out after one formation cycle at 0.1C in the voltage window of 2.5−4.25 V. EIS plots of all cathodes (d) before cycling and (e) after 100 cycles.

Table 2.4 Experimental results from electrochemical tests in Figure 2.12.

Sample	Coulombic efficiency in formation process at 0.1C [%]	Initial discharge capacity at 0.33C [mAh/g]	Retention at 0.33C [%]
SP_LL40	91.7	180.8	71.3
SWCNT_LL40	91.9	177.1	75.2
O-SWCNT_LL40	92.2	185.1	78.4

Sample	Pristine	After cycling	
	Charge transfer resistance [R_{ct}, Ω]	Film resistance [R_{SEI}, Ω]	Charge transfer resistance [R_{ct}, Ω]
SP_LL40	79	66	8
SWCNT_LL40	63	18	14
O-SWCNT_LL40	45	12	16

The composition of CEI layers on the cathode surface was analyzed before and after 100 cycles using X-ray photoelectron spectroscopy (XPS). The F 1s XPS spectra of the fresh and cycled dry-processed cathodes are presented in **Figure 2.13**. Prior to cycling, all F 1s signals originated from the PTFE binder **(Figure 2.13a)**. Following cycling, LiF and $Li_xPO_yF_z$ compounds were detected at 685.1 eV and 687.2 eV, respectively, which are known to result from electrochemical side reaction of $LiPF_6$ **(Figure 2.13b)**.[43] The results of electrochemical cycles were also detected in the C 1s XPS spectra displayed in **Figure 2.14**. The C 1s XPS spectra obtained after cycling displayed components such as C-C, C-O, and C=O, resulting from the electrochemical cycles.[44] All three cathodes exhibited similar behavior compared to their respective pristine states. In the SP-based dry-processed cathode, the amount of LiF and $Li_xPO_yF_z$ were the least calculated from the peak area. Since the SP did not completely cover the NCM811 active material, the electron transport in the electrode was insufficient, reducing the side reaction of the electrolyte itself. Conversely, both SWCNT and O-SWCNT dry-cathodes exhibited sufficient amounts of CEI components, and the peak area ratio of (LiF + $Li_xPO_yF_z$)/(LiF + $Li_xPO_yF_z$ + CF_2) of SWCNT and O-SWCNT dry-cathodes were 52.4% and 49.1%, respectively. As LiF and $Li_xPO_yF_z$ are recognized as electrical insulators, it can be seen that O-SWCNT enhances the coverage of the NCM811 cathode material by the oxygen functional group and suppresses the side reaction that generates F-contained CEI, resulting in the more interfacial stability than SWCNT. This may be another explanation for the superior electrochemical properties observed in O-SWCNT dry-cathodes,[45] in addition to their improved filling and affinity for NCM particles.

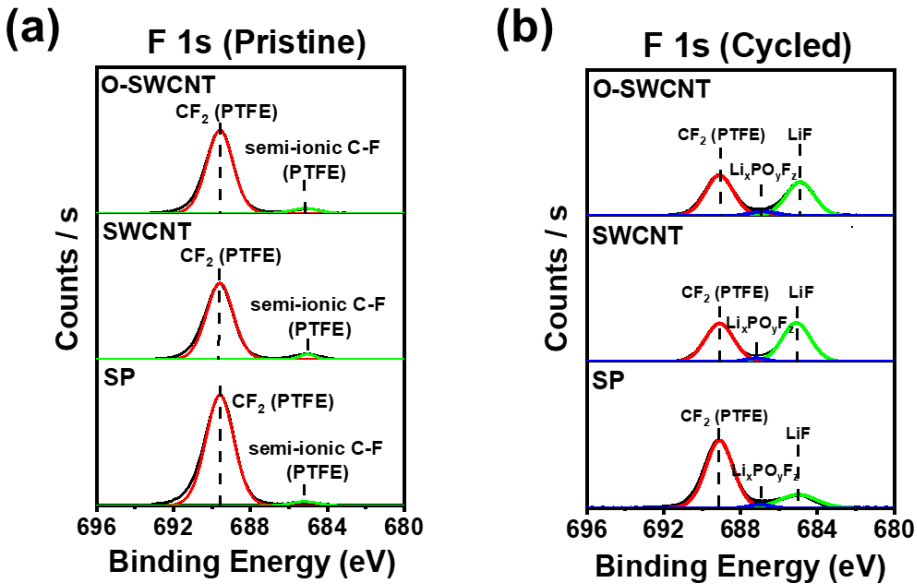

Figure 2.13 CEI analysis of cathodes at the loading level of 30 mg/cm^2 by XPS: F 1s XPS spectra (a) before cycling and (b) after 100 cycles.

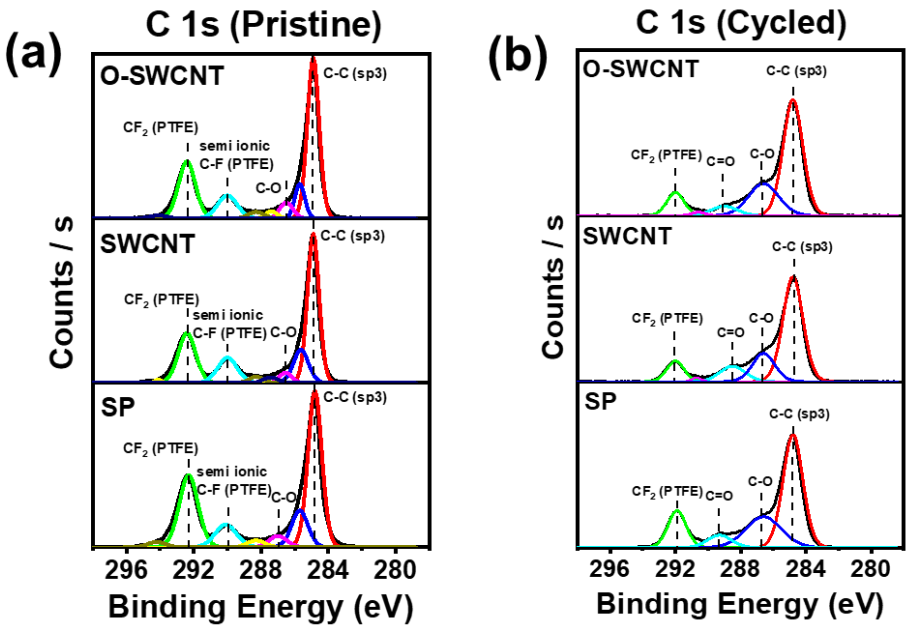

Figure 2.14 CEI analysis of cathodes at the loading level of 30 mg/cm^2 by XPS: C 1s XPS spectra (a) before cycling and (b) after 100 cycles.

To explore the outcomes of electrochemical reactions in greater depth, cross-sectional SEM images of all cathodes were obtained **(Figure 2.15a-f)**. Lower magnification images are available in **Figure 2.16**. Following 100 cycles, the majority of NCM811 particles in the SP-based dry-processed cathode exhibited microcracks, as illustrated in **Figures 2.15b and 2.16b**. In contrast, the SWCNT and O-SWCNT-based cathodes did not demonstrate the development of such microcracks **(Figures 2.15d, 2.15f, 2.16d, and 2.16f)**. The formation of microcracks in the Ni-rich NCM materials occurs along the grain boundary in secondary particles because of the transition from the H2 phase to the H3 phase near ~4.1 V vs. Li/Li^+, which is accompanied with anisotropic volume change of the lattice structure.[46,47,48,49] In accordance to the microcrack formation, an irreversible redox behavior was detected in the dQ/dV plots of the SP-based cathode **(Figure 2.15g)**; after 50 cycles, the peak at ca. 4.1 V in the reverse process diminished. Conversely, the two SWCNT cathodes maintained reversibility even after 100 cycles **(Figures 2.15h, 2.15i)**. These distinct results among the different cathodes can be interpreted in link to recent findings that surface coating[50, 51] of the active material or high surface coverage of the active material by binder[52, 53] alleviate the microcrack formation in Ni-rich cathode materials by preventing the penetration of the electrolyte into the secondary particles of the cathode active material.[54, 55] It is thought that the incorporation of even a small amount of SWCNT, which possesses a higher specific surface area than SP, can effectively cover the cathode active material particles to protect their interface against the penetration of the electrolyte. Furthermore, the stress experienced by particles during cycles could have been largely released by the SWCNT matrices with elasticity.

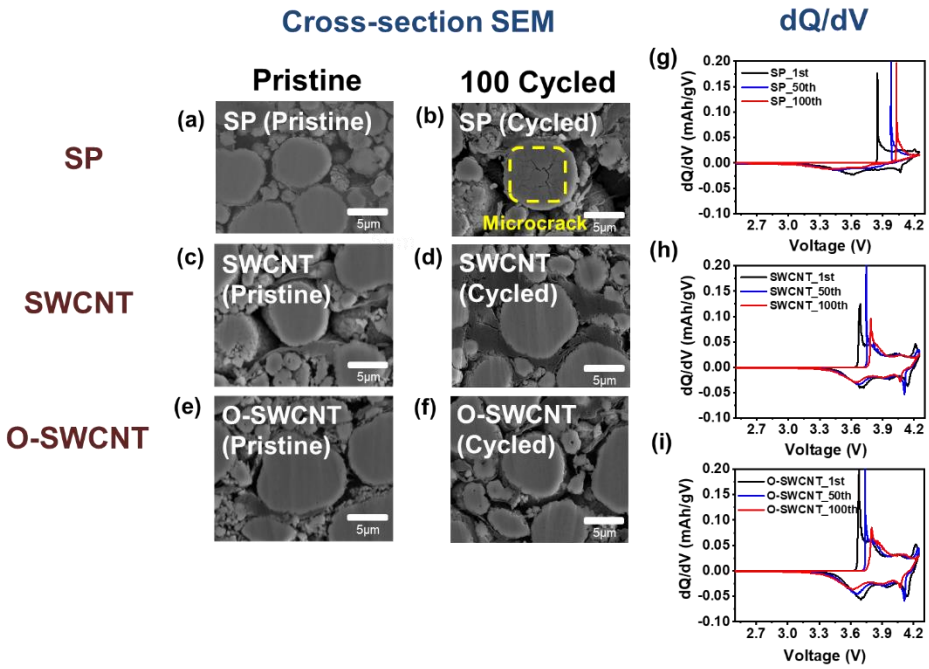

Figure 2.15 Cross-sectional SEM images of SP (a,b), SWCNT (c,d), O-SWCNT (e,f) cathodes at the loading level of 30 mg/cm^2: (a,c,e) Before cycling and (b,d,f) after 100 cycles. dQ/dV plots of SP (g), SWCNT (h), O-SWCNT (i) cathodes in the 1st, 50th, 100th cycles.

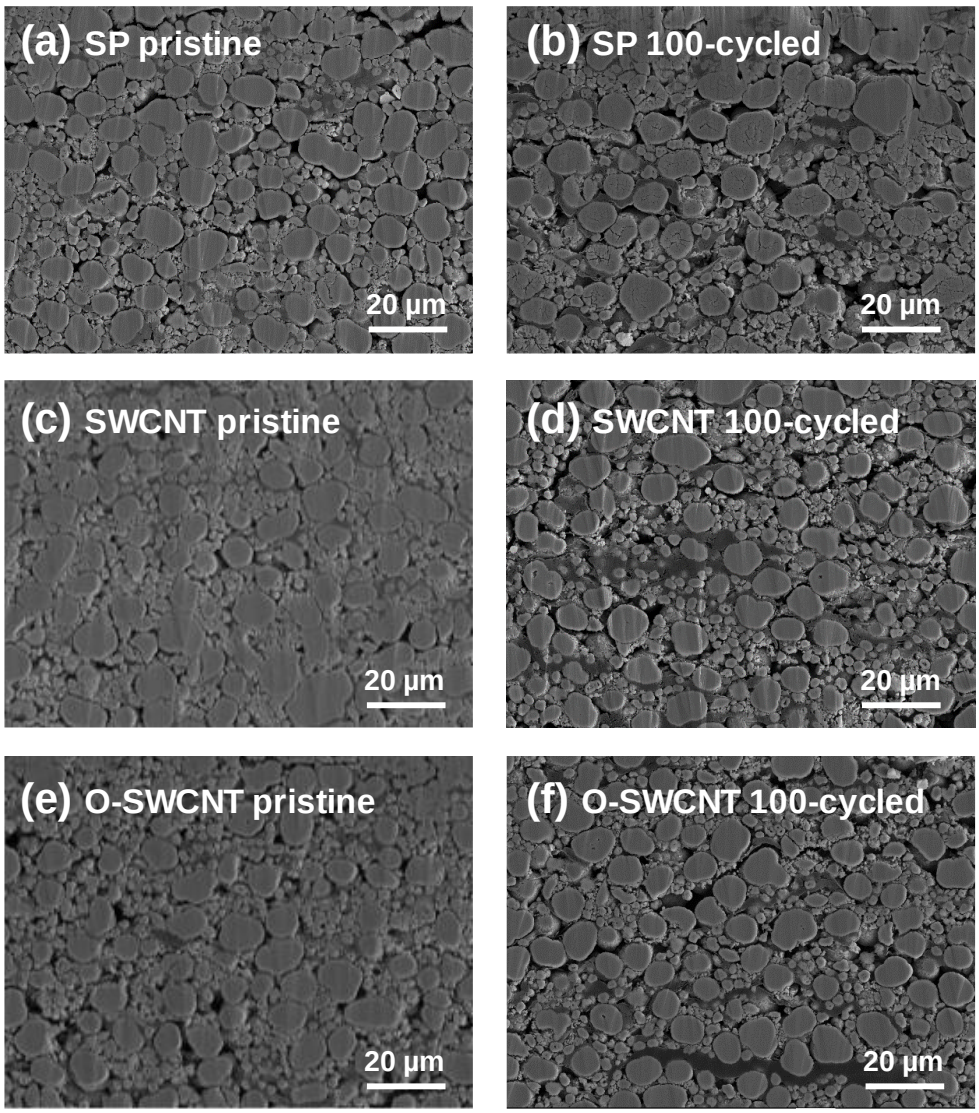

Figure 2.16 Low-magnification cross-sectional SEM images of SP (a,b), SWCNT (c,d), O-SWCNT (e,f) cathodes at the loading level of 30 mg/cm^2: (a,c,e) Before cycling and (b,d,f) after 100 cycles.

2.4. References

[1] J. M. Tarascon, *Philos. Trans. R. Soc. A-Math. Phys. Eng. Sci.* **2010**, *368* (1923), 3227-3241.

[2] J. Xie and Y. C. Lu, *Nat. Commun.* **2020**, *11* (1), 2499.

[3] S. Dühnen, J. Betz, M. Kolek, R. Schmuch, M. Winter and T. Placke, *Small Methods* **2020**, *4* (7), 2000039.

[4] M. Díaz-Ramírez, V. Ferreira, T. García-Armingol, A. López-Sabirón and G. Ferreira, *Sustainability* **2020***, 12 (1)*, 342.

[5] D. L. Wood, M. Wood, J. Li, Z. Du, R. E. Ruther, K. A. Hays, N. Muralidharan, L. Geng, C. Mao and I. Belharouak, *Energy Storage Mater.* **2020**, *29*, 254-265.

[6] K. G. Gallagher and P. A. Nelson, 6 - Manufacturing Costs of Batteries for Electric Vehicles. In *Lithium-Ion Batteries*, Pistoia, G. Ed.; Elsevier, 2014; pp 97-126.

[7] L. Mauler, F. Duffner, W. G. Zeier and J. Leker, *Energy Environ. Sci.* **2021**, *14* (9), 4712-4739.

[8] Y. Liu, R. Zhang, J. Wang and Y. Wang, *iScience* **2021**, *24* (4), 102332.

[9] D. L. Wood, J. Li and C. Daniel, *J. Power Sources* **2015**, *275*, 234-242.

[10] S. Ahmed, P. A. Nelson, K. G. Gallagher and D. W. Dees, *J. Power Sources* **2016**, *322*, 169-178.

[11] R. Sliz, J. Valikangas, H. Silva Santos, P. Vilmi, L. Rieppo, T. Hu, U. Lassi and T. Fabritius, *ACS Appl. Energ. Mater.* **2022**, *5* (4), 4047-4058.

[12] F. Font, B. Protas, G. Richardson and J. M. Foster, *J. Power Sources* **2018**, *393*, 177-185.

[13] B. Westphal, H. Bockholt, T. Günther, W. Haselrieder and A. Kwade, *ECS Trans.* **2015**, *64* (22), 57.

[14] Y. Lu, C.-Z. Zhao, H. Yuan, J.-K. Hu, J.-Q. Huang and Q. Zhang, *Matter* **2022**, *5* (3), 876-898.

[15] J. Shin, J.-H. Lee, J. K. Seo, W. T. A. Ran, S. M. Hwang and Y.-J. Kim, *Int. J. Energy Res.* **2022**, *46* (11), 16061-16074.

[16] H. Duong, A. Suszko and H. Feigenbaum, (Invited) Dry Electrode Process Technology. *ECS Meeting Abstracts.* 2016, *MA2016-01* (5), 475.

[17] R. Dominko, M. Gaberscek, J. Drofenik, M. Bele, S. Pejovnik and J. Jamnik, *J. Power Sources* **2003**, *119-121*, 770-773.

[18] J. K. Mayer, L. Almar, E. Asylbekov, W. Haselrieder, A. Kwade, A. Weber and H. Nirschl, *Energy Technol.* **2019**, *8* (2), 1900161.

[19] D. Grießl, K. Huber, R. Scherbauer and A. Kwade, *Adv. Powder Technol.* **2021**, *32* (7), 2280-2288.

[20] M. F. L. De Volder, S. H. Tawfick, R. H. Baughman and A. J. Hart, *Science* **2013**, *339* (6119), 535-539.

[21] T. W. Ebbesen, H. J. Lezec, H. Hiura, J. W. Bennett, H. F. Ghaemi and T. Thio, *Nature* **1996**, *382* (6586), 54-56.

[22] Y. Liu, X. Li, H. Guo, Z. Wang, W. Peng, Y. Yang and R. Liang, *J. Power Sources* **2008**, *184* (2), 522-526.

[23] Y. Mi, P. Gao, W. Liu, W. Zhang and H. Zhou, *J. Power Sources* **2014**, *267*, 459-468.

[24] K. Sheem, Y. H. Lee and H. S. Lim, *J. Power Sources* **2006**, *158*, 1425-1430.

[25] I. A. Kinloch, J. Suhr, J. Lou, R. J. Young and P. M. Ajayan, *Science* **2018**, *362* (6414), 547-553.

[26] S. Wang, Z. Huang, W. Shi, D. Lee, Q. Wang, W. Shang, Y. Stein, Y. Shao-Horn, T. Deng, B. L. Wardle and K. Cui, *ACS Appl. Mater. Interfaces* **2021**, *13* (24), 28583-28592.

[27] S. Maruyama, E. Einarsson, Y. Murakami and T. Edamura, *Chem. Phys. Lett.* **2005**, *403* (4-6), 320-323.

[28] K. A. Worsley, I. Kalinina, E. Bekyarova and R. C. Haddon, *J. Am. Chem. Soc.* **2009**, *131* (50), 18153-18158.

[29] R. J. Headrick, S. M. Williams, C. E. Owens, L. W. Taylor, O. S. Dewey, C. J. Ginestra, L. Liberman, A. M. Ya'akobi, Y. Talmon, B. Maruyama, G. H. McKinley, A. J. Hart and M. Pasquali, *Sci. Adv.* **2022**, *8* (17), eabm3285.

[30] G. Stando, S. Han, B. Kumanek, D. Łukowiec and D. Janas, *Sci Rep* **2022**, *12* (1), 4358.

[31] C. Wei, B. Akinwolemiwa, Q. Wang, L. Guan, L. Xia, D. Hu, B. Tang, L. Yu and G. Z. Chen, *Adv. Sustain. Syst.* **2019**, *3* (11), 1900065.

[32] S. W. Lee, B. M. Gallant, Y. Lee, N. Yoshida, D. Y. Kim, Y. Yamada, S. Noda, A. Yamada and Y. Shao-Horn, *Energy Environ. Sci.* **2012**, *5* (1), 5437-5444.

[33] M. M. Falinski, E. M. Albalghiti, A. Backhaus and J. B. Zimmerman, *ChemSusChem* **2020**, *14* (3), 898-908.

[34] M. Ryu, Y.-K. Hong, S.-Y. Lee and J. H. Park, *Nat. Commun.* **2023**, *14* (1), 1316.

[35] M. S. Dresselhaus, G. Dresselhaus, R. Saito, A. Jorio, *Phys. Rep.* **2005**, *409* (2), 47-99.

[36] J. Gelb, D. P. Finegan, D. J. L. Brett and P. R. Shearing, *J. Power Sources* **2017**, *357*, 77-86.

[37] P. P. Pal, T. Larionova, I. V. Anoshkin, H. Jiang, M. Nisula, A. A. Goryunkov,

O. V. Tolochko, M. Karppinen, E. I. Kauppinen and A. G. Nasibulin, *J. Phys. Chem. C* **2015**, *119* (49), 27821-27828.

[38] J. H. Kim, J. Ahn, H.-M. Kim, J. Y. Cho, D. G. Lee, Y. Oh, J. H. Park, J. S. Kim, J.-K. Yoo and J. T. Han, *Chem. Eng. J.* **2023**, *458*, 141350.

[39] M. M. Falinski, E. M. Albalghiti, A. Backhaus and J. B. Zimmerman, *ChemSusChem* **2020**, *14* (3), 898-908.

[40] W. Choi, H.-C. Shin, J. M. Kim, J.-Y. Choi and W.-S. Yoon, *J. Electrochem. Sci. Technol.* **2020**, *11* (1), 1-13.

[41] J. Kang, J. Wen, S. H. Jayaram, A. Yu and X. Wang, *Electrochim. Acta* **2014**, *115*, 587-598.

[42] M. Wang, R. Zhang, Y. Gong, Y. Su, D. Xiang, L. Chen, Y. Chen, M. Luo and M. Chu, *Solid State Ion.* **2017**, *312*, 53-60.

[43] A. M. Andersson, D. P. Abraham, R. Haasch, S. MacLaren, J. Liu and K. Amine, *J. Electrochem. Soc.* **2002**, *149* (10), A1358.

[44] N. Schulz, R. Hausbrand, C. Wittich, L. Dimesso and W. Jaegermann, *J. Electrochem. Soc.* **2018**, *165* (5), A833.

[45] G. Yang, J. Shi, C. Shen, S. Wang, L. Xia, H. Hu, H. Luo, Y. Xia and Z. Liu, *RSC Adv.* **2017**, *7*, 26052-26059.

[46] F. Wu, N. Liu, L. Chen, Y. Su, G. Tan, L. Bao, Q. Zhang, Y. Lu, J. Wang, S. Chen and J. Tan, *Nano Energy* **2019**, *59*, 50-57.

[47] H.-H. Ryu, K.-J. Park, C. S. Yoon and Y.-K. Sun, *Chem. Mat.* **2018**, *30* (3), 1155-1163.

[48] A. O. Kondrakov, A. Schmidt, J. Xu, H. Geßwein, R. Mönig, P. Hartmann, H. Sommer, T. Brezesinski and J. Janek, *J. Phys. Chem. C* **2017**, *121* (6), 3286-3294.

[49] J.-M. Lim, T. Hwang, D. Kim, M.-S. Park, K. Cho and M. Cho, *Sci Rep* **2017**, *7* (1), 39669.

[50] B. Song, W. Li, S.-M. Oh and A. Manthiram, *ACS Appl. Mater. Interfaces* **2017**, *9* (11), 9718-9725.

[51] Z. Chen, Y. Qin, K. Amine and Y. K. Sun, *J. Mater. Chem.* **2010**, *20* (36), 7606-7612.

[52] B. Chang, J. Kim, Y. Cho, I. Hwang, M. S. Jung, K. Char, K. T. Lee, K. J. Kim and J. W. Choi, *Adv. Energy Mater.* **2020**, *10* (29), 2001069.

[53] S. Jeong, S. Young Park, B. So, K. Tae Lee, Y. Don Park and J. Mun, *Chem. Eng. J.* **2022**, *448*, 137654.

[54] D. J. Miller, C. Proff, J. G. Wen, D. P. Abraham and J. Bareño, *Adv. Energy Mater.* **2013**, *3* (8), 1098-1103.

[55] H.-H. Sun and A. Manthiram, *Chem. Mater.* **2017**, *29* (19), 8486-8493.

Chapter 3. PVdF-Assisted Ceramic/Polymer Hybrid Solid Electrolyte by *in situ* Crosslinking for Lithium Metal Solid State Batteries

3.1. Introduction

In recent years, the size of Lithium-ion batteries (LIBs) has grown significantly, necessitating the fulfillment of both high energy density and safety requirements. In particular, all-solid-state batteries have received considerable attention because they can be used with low-flammable inorganic solid electrolytes to complement LIBs that use organic electrolytes. Solid electrolytes serve as a separator between the positive and negative electrodes, enabling the flow of ions but preventing the flow of electrons. Several types of inorganic solid electrolytes, including sulfides[1, 2, 3, 4], oxides[5, 6, 7], polymers[8, 9]and hydrides[10], have been discovered over the past decades. Specifically, solid oxide electrolytes have demonstrated promising conductivity, high chemical stability, and mechanical properties, suggesting that they can operate at high voltages of ≥4.3 V. This makes them more favorable than sulfide solid electrolytes since they have a wider electrochemical window.[11] However, they are sensitive to moisture, and they exhibit Li^+/H^+ exchange at room temperature, resulting in the formation of lithiophobic Li_2CO_3. [12] Furthermore, the inability of the rigid particles to fill the pores of the electrolyte layer results in hindered lithium-ion conduction and high resistance at both the grain boundaries and the electrolyte–

electrode interfacial region.[13] Another significant hurdle to the commercialization of oxide solid electrolytes is that high-temperature treatments (above 1000 °C) are required for their production.[14]

To address these challenges, researchers have shifted their focus toward a thick- or thin-film approach that uses a combination of solid oxide electrolytes and solid polymer electrolytes (PEs), such as poly(ethylene oxide) (PEO), rather than pellet-type all-solid-state batteries.[15, 16] This approach utilizes the slurry-based wet electrode process for lithium secondary batteries, which allows for the creation of a composite film by mixing a solid electrolyte and a PE. Additionally, it has the advantage of not requiring an additional sintering process since the polymer fills the voids of the solid electrolyte. However, when PEO is used as a polymer, it must overcome the problems of low ionic conductivity at room temperature and a narrow electrochemical window.[17]

This study focuses on the development of a method for preparing organic/inorganic hybrid solid electrolytes (HSEs) in the form of thick films. An in situ cross-linkable polymer, namely, poly(ethylene glycol) diacrylate (PEGDA), was incorporated into a sodium (Na) superionic conductor (NASICON)-based solid oxide electrolyte, which resulted in ionic conductivities that were comparable to those of pure solid electrolytes in a significantly short period.[18]

Furthermore, this study demonstrates that the incorporation of poly(vinylidene fluoride) (PVdF), a polymer with a high dielectric constant, reduces the crystallinity of PEO.[19, 20] Consequently, this enhances the physical characteristics of the mixed solid electrolyte and increases the ionic conductivity. Importantly, this study emphasizes that the characteristics of mixed solid electrolytes are significantly influenced by the properties of the polymers used.

3.2. Experimental Methods

Preparation of the PE solution and HSE film: The PE solution was prepared by mixing PEGDA (M_n = 700, Sigma-Aldrich) and lithium salt, lithium bis(trifluoromethanesulfonyl)imide (LiTFSI, 99.9%, Sigma-Aldrich) salt in a weight ratio of 1:1 (the ratio of ether oxygen to lithium was 5:1). Prior to mixing, the LiTFSI salt was completely dissolved in an N-methyl-2-pyrrolidone (NMP) solvent, and then PVdF was added to the PE solution. Next, NASICON-type Li_2O–SiO_2–TiO_2–P_2O_5 (LSTP, JEONGKWAN Co., Ltd., Korea) solid electrolyte, the PE solution, and 2 wt% of a 2,2′-azobisisobutyronitrile (AIBN; Junsei, Japan) thermal initiator were mixed with the slurry for the HSE using a planetary centrifugal mixer (Thinky mixer, AR-100, Japan) for 5 min. The as-prepared AIBN was recrystallized from methanol and stored in a refrigerator. Subsequently, the slurry was cast onto an Al foil using the doctor blade technique and then heated on a hot plate at 60 °C for 1 h in an Ar-filled glove box to inhibit moisture. Finally, the HSE was calendered via roll pressing to adjust its thickness to 40–50 μm.

Material characterization: Ionic conductivity was measured using the electrochemical impedance spectroscopy (EIS) technique and a battery cycler (VSP, Bio-Logic, France) with a symmetric cell configuration. The Al foil served as a blocking electrode. Alternating current (AC) was applied at a frequency range of 1 MHz to 0.1 Hz. After obtaining the Nyquist plot, the ionic conductivity was determined with the total resistance using the following equation (3.1):

$$\sigma = \frac{L}{RA}, \qquad (3.1)$$

where σ is the ionic conductivity, R is the total resistance, *L* is the thickness of the material, and *A* is the area of the material.

Characteristic chemical bonds were examined using Fourier-transform infrared spectroscopy (FT-IR) (TENSOR27, Bruker, USA) with a resolution of 4 cm^{-1}. Thermal properties of PE and HSE were analyzed using differential scanning calorimetry (DSC, Discovery DSC, TA instrument, USA). The crystallization temperature (T_c) was measured at a rate of 10 °C/min. The electrochemical window of the HSE was examined by preparing cells with a SUS|HSE layer|Li configuration and performing linear sweep voltammetry (LSV) scans in a potential range of 3.0–6.0 V vs. Li/Li^+ at a rate of 0.5 mV/s.

Electrochemical Characterization: The electrochemical cell was assembled with a CR2032-type coin cell in an Ar-filled glove box. Each cycle was performed in a constant current charge/discharge mode within a potential range of 2.7–4.2 V (vs Li/Li^+) at 60 °C. Cathode slurries were prepared by mixing NCM811, super P, and PVdF in NMP at a weight ratio of 80:10:10. The slurry of each cathode was cast onto the Al foil using the doctor blade technique and then dried at 60 °C for 12 h. The cathode loading level was about 3 mg/cm^2. A lithium metal with a thickness of ~150 μm (Honjo metal, Japan) was used as the anode. Additionally, about 3 μL of 1 M $LiPF_6$ in an EC/DMC=1:1 (Soulbrain, South Korea) electrolyte was added to the anode and cathode to reduce the interfacial resistance. All electrochemical cells were allowed to rest for 12 h to ensure that the cathodes were sufficiently wetted with the electrolyte prior to electrochemical testing. CC/CV and CC modes were adopted for the charging and discharging processes, respectively, using a battery cycler (WBCS3000L, WonAtech, South Korea). Prior to cycling, the forming process was

performed for one cycle at 0.1 C under a cutoff condition of 0.01 C. Cycle tests were performed at 0.5 C under a cutoff condition of 0.05 C using the abovementioned molding process. EIS analysis was performed with AC over a frequency range of 0.01 Hz to 1 MHz at 25 °C and a voltage perturbation of 10 mV using a potentiostat (VSP, Bio-logic, France). The resulting Nyquist plot was fitted to an equivalent circuit using EC-Lab software.

3.3. Results and Discussion

The HSE films were synthesized using a slurry-casting method, followed by a thermal curing process. These procedures are explained in detail in the experimental section and illustrated in **Figure 3.1**. An Al|HSE|Al symmetric cell was assembled to determine the optimal LSTP and PE compositions for the HSE. The ionic conductivity was then measured using EIS. The optimal ionic conductivity was observed when the weight ratio of LSTP and PE was 70:30 **(Figure 3.2)**. The ionic conductivity was observed to decrease when the LSTP amount exceeded 70 wt%, indicating that the mediator between the particles was insufficient to enable the transfer of lithium ions.[21] The trend in ion conductivity was examined by varying the PVdF content of the binder while maintaining the optimal LSTP/PE ratio of 70:30, and it was observed that the ideal PVdF content was 5 wt% **(Figure 3.3)**. To investigate the reasons for the aforementioned results, the thermal properties of the HSE were examined through DSC analysis, as shown in **Figure 3.4**. The crystallinity of HSEs can be determined by calculating the relative enthalpy based on the peak area observed near the crystallization temperature. In particular, the lower the enthalpy, the lower the crystallinity of the polymer, particularly when PVdF is present at a concentration of 5 wt%. Furthermore, the electrochemical window at room temperature results obtained via LSV showed an improvement in the electrochemical oxidation stability due to the decreased crystallinity of the polymer, as shown in **Figure 3.5a**. Additionally, the Arrhenius plot analysis revealed a decrease in the activation energy value obtained from the slope, as illustrated in **Figure 3.5b**.

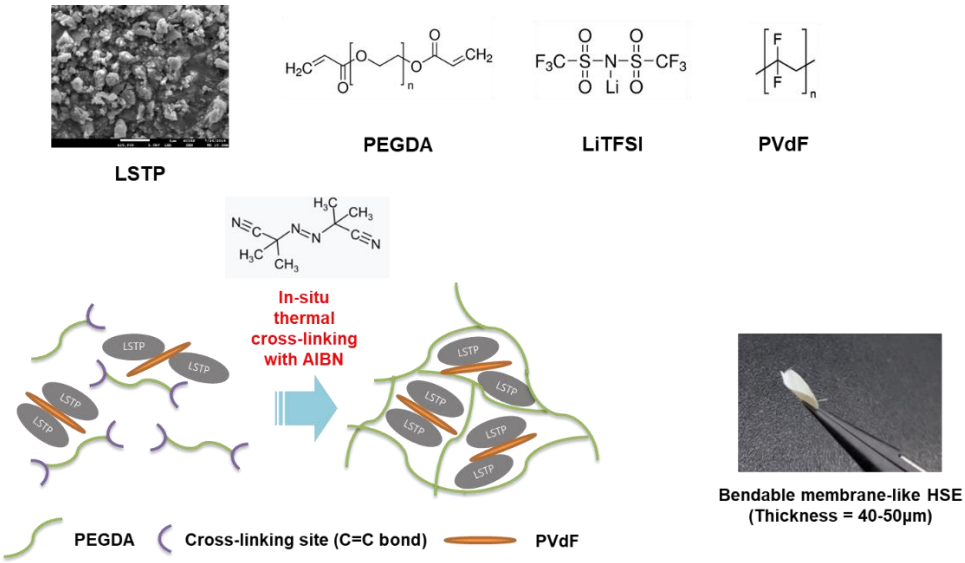

Figure 3.1 Schematic illustration of HSE preparation.

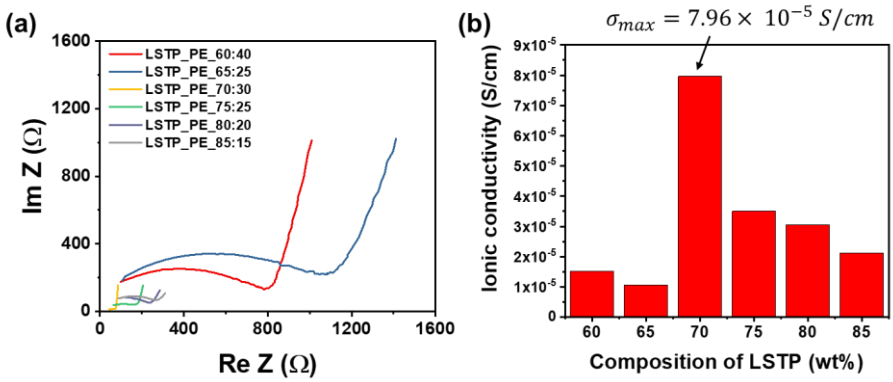

Figure 3.2 (a) EIS plots according to the ratio of LSTP and PE. (b) Ionic conductivity of all HSEs were calculated by Equation (3.1).

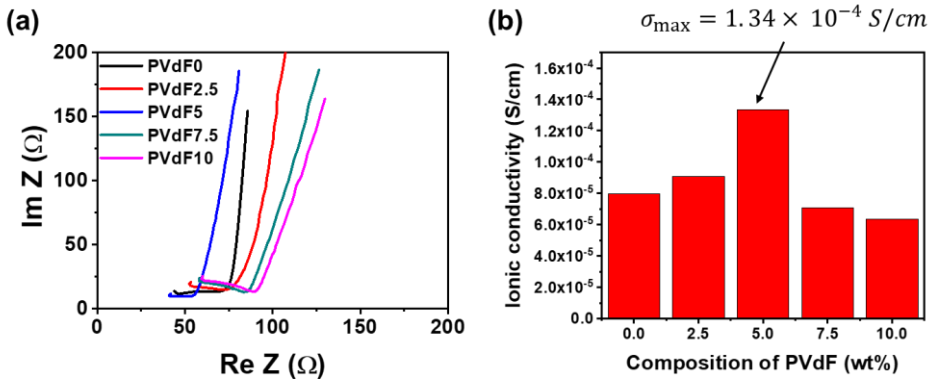

Figure 3.3 (a) EIS plots according to the ratio of PVdF. The ratio of LSTP to PE was 70:30. (b) Ionic conductivity of all HSEs were calculated by Equation (3.1).

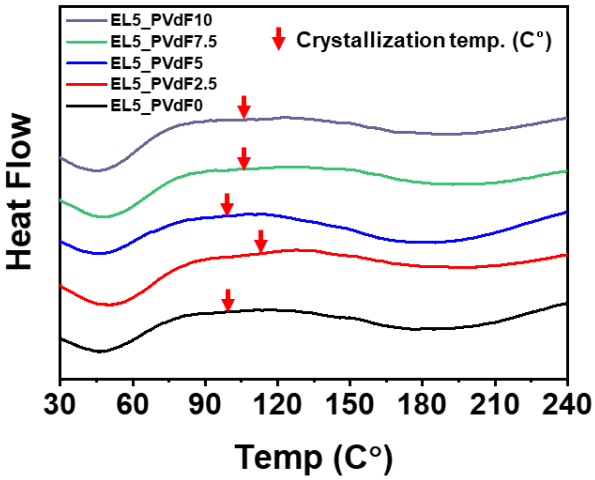

Sample	Enthalpy (J/g)
PVdF0	5.066
PVdF2.5	5.344
PVdF5	**3.485**
PVdF7.5	5.397
PVdF10	5.432

Figure 3.4 DSC analysis and relative enthalpy values of HSE according to the content of PVdF.

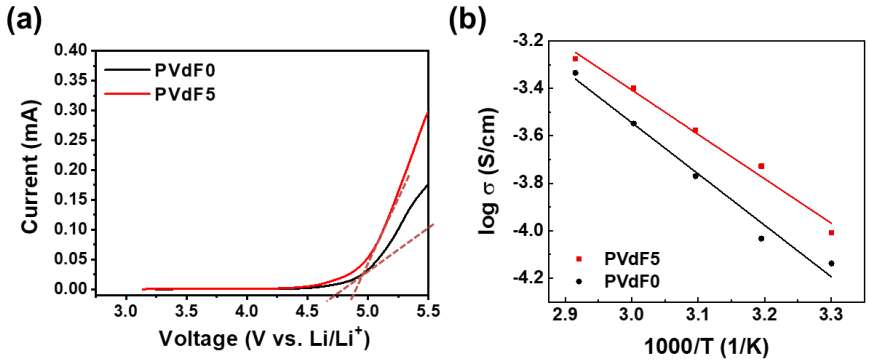

Figure 3.5 (a) Electrochemical window result of HSE determined by LSV (scan rate = 0.5 mV/s) at room temperature. (b) Arrhenius plot result of HSE in the temperature range of 30–60°C.

Lithium half-cell tests were conducted at 60 °C to examine the electrochemical properties of the HSE. During the formation cycle at 0.1 C, the PVdF5 solid electrolyte had slightly higher coulombic efficiency (84.9%) than PVdF0 (82.1%), as depicted in **Figure 3.6a**. In the cycle life test at 0.5 C, the capacity retention rate of PVdF5, based on the 100th discharge capacity, was ~10% higher than that of PVdF0, as illustrated in **Figure 3.6b**. Furthermore, during the Li stripping/plating test conducted at a current density of 0.3 mA/cm^2, the operating time of PVdF5 was approximately twice as long as that of PVdF0 without short-circuiting, as shown in **Figure 3.7**. It is worth noting that these results are attributed to the inclusion of a small amount of electrolyte in the electrochemical cell. The interfacial resistance between the electrode and electrolyte is expected to be high without the electrolyte, highlighting the need for further research on electrode design, particularly for the anode, to mitigate this issue.

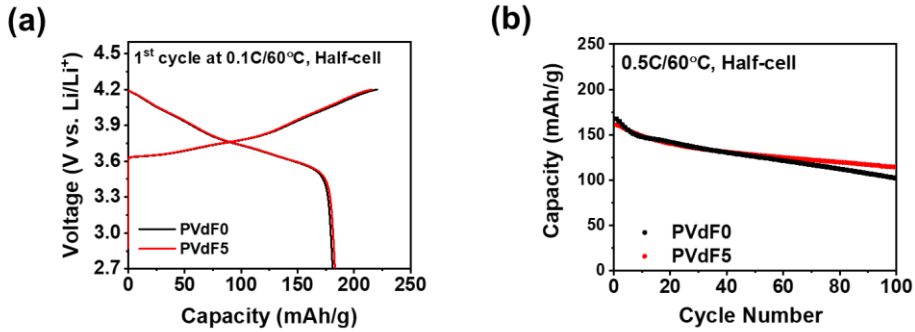

HSE film	Charge (mAh/g)	Discharge (mAh/g)	Eff. (%)
PVdF0	220.6	181.1	82.1
PVdF5	**215.8**	**183.2**	**84.9**

HSE film	Discharge capacity @ 100th cycle (mAh/g)	Retention @ 100th cycle (%)
PVdF0	102.0	60.9
PVdF5	**114.5**	**71.1**

Figure 3.6 Electrochemical performance applied all HSEs at 60°C in half-cell configurations. (a) Voltage profiles in first formation cycle (1C = 200 mA/g). (b) Cycling tests measured at 0.5C.

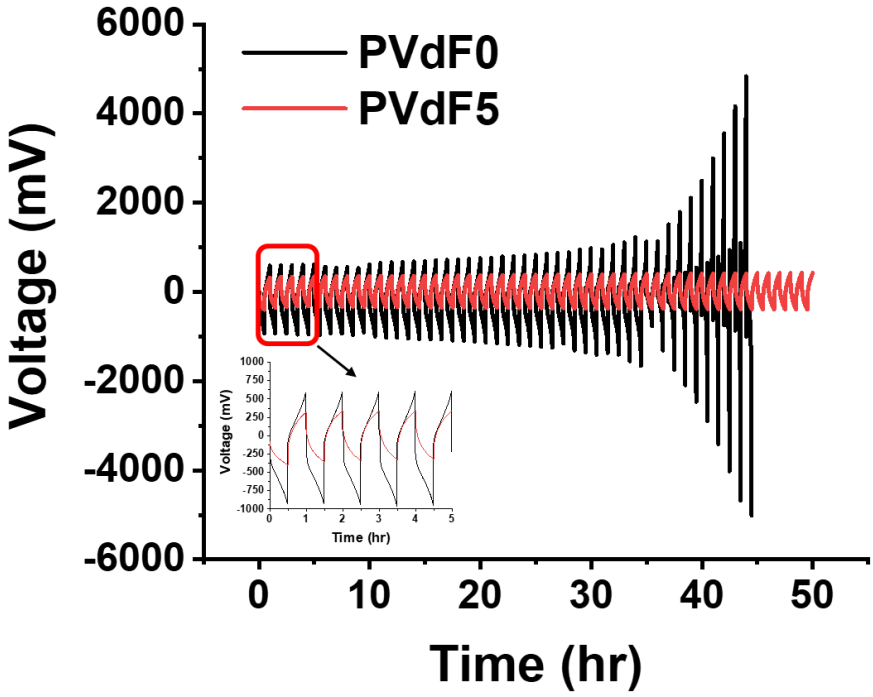

Figure 3.7 Li plating/stripping test at 60°C in the current density of 0.3 mA/cm^2.

3.4. References

[1] H.-J. Deiseroth, S.-T. Kong, H. Eckert, J. Vannahme, C. Reiner, T. Zaiß and M. Schlosser, *Angew. Chem., Int. Ed.* **2008**, *47* (4), 755– 758.

[2] N. Kamaya, K. Homma, Y. Yamakawa, M. Hirayama, R. Kanno, M. Yonemura, T. Kamiyama, Y. Kato, S. Hama and K. Kawamoto, *Nat. Mater.* **2011**, *10* (9), 682– 68.

[3] M. A. Kraft, S. P. Culver, M. Calderon, F. Böcher, T. Krauskopf, A. Senyshyn, C. Dietrich, A. Zevalkink, J. Janek and W. G. Zeier, *J. Am. Chem. Soc.* **2017**, *139* (31), 10909– 10918.

[4] R. C. Xu, X. L. Wang, S. Z. Zhang, Y. Xia, X. H. Xia, J. B. Wu and J. P. Tu, *J. Power Sources* **2018**, *374*, 107– 112.

[5] R. Murugan, V. Thangadurai and W. Weppner, *Angew. Chem., Int. Ed.* **2007**, *46* (41), 7778– 7781.

[6] X. Xu, Z. Wen, X. Yang, J. Zhang and Z. Gu, *Solid State Ion.* **2006**, *177* (26), 2611-2615.

[7] R. Takano, K. Tadanaga, A. Hayashi and M. Tatsumisago, *Solid State Ion.* **2014**, *255*, 104-107.

[8] Z. Gadjourova, Y. G. Andreev, D. P. Tunstall and P. G. Bruce, *Nature* **2001**, *412*, 520-523.

[9] Z. Xue, D. He and X. Xie, *J. Mater. Chem. A* **2015**, *3*, 19218-19253.

[10] A. Unemoto, M. Matsuo and S.-i. Orimo, *Adv. Funct. Mater.* **2014**, *24*, 2267-2279.

[11] B. V. Lotsch and J. Maier, *J. Electroceramics* **2017**, *38*, 128-141.

[12] H. Huo, J. Luo, V. Thangadurai, X. Guo, C.-W. Nan and X. Sun, *ACS Energy Let.* **2020**, *5*, 252-262.

[13] L. Cheng, E. J. Crumlin, W. Chen, R. Qiao, H. Hou, S. Franz Lux, V. Zorba, R. Russo, R. Kostecki, Z. Liu, K. Persson, W. Yang, J. Cabana, T. Richardson, G. Chen and M. Doeff, *Phys. Chem. Chem. Phys.* **2014**, *16*, 18294-18300.

[14] W. Xue, Y. Yang, Q. Yang, Y. Liu, L. Wang, C. Chen and R. Cheng, *RSC Adv.* **2018**, *8*, 13083-13088.

[15] L. Chen, Y. Li, S.-P. Li, L.-Z. Fan, C.-W. Nan and J. B. Goodenough, *Nano Energy* **2018**, *46*, 176-184.

[16] F. Chen, D. J. Yang, W. P. Zha, B. D. Zhu, Y. H. Zhang, J. Y. Li, Y. P. Gu, Q. Shen, L. M. Zhang and D. R. Sadoway, *Electrochim. Acta* **2017**, *258*, 1106-1114.

[17] K. Nie, X. Wang, J. Qiu, Y. Wang, Q. Yang, J. Xu, X. Yu, H. Li, X. Huang and L. Chen, *ACS Energy Lett.* **2020**, *5*, 826-832.

[18] A. F. Visentin and M. J. Panzer, *ACS Appl. Mater. Interfaces* **2012**, *4*, 2836-2839.

[19] J. E. Lee, Y. Guo, R. E. Lee and S. N. Leung, *RSC Adv.* **2017**, *7*, 48712-48722.

[20] M. N. Tamaño-Machiavello, C. M. Costa, J. Molina-Mateo, C. Torregrosa-Cabanilles, J. M. Meseguer-Dueñas, S. N. Kalkura, S. Lanceros-Méndez, R. Sabater i Serra and J. L. Gómez Ribelles, *Mater. Today Commun.* **2015**, *4*, 214-221.

[21] H. Huo, Y. Chen, J. Luo, X. Yang, X. Guo and X. Sun, *Adv. Energy Mater.* **2019**, 1804004.

Chapter 4. Summary

This dissertation shows that conductivity improvement is key to designing a new process for realizing high energy density lithium-ion batteries.

In chapter 2, dry-processed high-nickel cathodes can exhibit satisfactory electrochemical properties even at an areal cathode loading of 30 mg/cm^2 or greater by incorporating SWCNT conductive agents with the proper surface functionalities. For such purpose, gas-phase ozone treatment has been introduced for SWCNTs, resulting in a complete dry-process for cathode fabrication without using a single drop of solvent. Compared to the conventional CB-based cathode counterpart, this ozone treatment of SWCNTs increased the affinity for NCM811 particles towards denser microstructures within the cathode composite as well as protected the CEI from unwanted side reactions during repeated charge-discharge cycles, which also contributed to mitigating the fatal microcrack formation in NCM811 particles. The study uncovers new opportunities of the emerging dry-electrode process for EV-targeted LIB manufacturing by employing carbon nanomaterials with the well-controlled surface chemistry.

In chapter 3, adding PVdF to the mixture of LSTP and PEGDA/LiTFSI polymers in the HSE led to a reduction in crystallinity, which improved the ionic conductivity and physical properties. This advancement enables the production of solid electrolyte membranes in a short timeframe. Furthermore, improvements in these physicochemical properties lead to improvements in electrochemical performance, increasing the possibility of expanding the use of solid oxide electrolytes.

국문초록

리튬 이온 전지는 스마트폰에서 전기 자동차에 이르기까지 많은 전자 장치에서 중요한 구성 요소로 자리잡고 있다. 중대형 전지의 개발에 따라 더 높은 에너지 밀도를 가진 전지를 구현하기 위한 주요 과제 중 하나는 전지 내에서 효율적이고 빠른 전하 전달을 달성하는 것이다. 전해액에서의 이온 전도도와 전극에서의 전기 전도도는 전하가 배터리를 통과할 수 있는 속도를 결정하는 주요 요소로써 배터리의 성능 향상을 위한 중요한 물리량이며, 낮은 전도도는 에너지 효율 감소, 배터리 수명 감소, 전력 출력 감소로 이어질 수 있다. 많은 연구진은 전도도가 높은 신소재 개발, 전하의 이동 거리를 최소화하기 위한 배터리 설계 최적화, 불순물을 줄이기 위한 제조 공정 개선 등 오랫동안 전도도 개선과 관련된 다양한 기술을 연구해왔다. 본 논문에서는 건식 전극 및 산화물계 고체 전해질 분야에서의 공정 개선에 있어서 전도도 튜닝의 중요성을 제안한다.

제 1 장에서는 전도도에 대한 간단한 이론적 배경과 함께 전도성 튜닝의 중요성을 소개한다. 제 2 장에서는 도전재로 오존 처리된 CNT 를 사용할 경우 하이니켈 양극활물질(NCM811)을 사용한 고로딩(30 mg/cm^2 이상) 건식 양극의 전기화학적 성능을 더욱 향상시킬 수 있음을 보여준다. 제 3 장에서는 물리적 특성 및 전기화학적 성능이 우수한 유/무기 하이브리드 고체 전해질 막의 제조 방법을 제시한다. 이는 유전 상수가 높은 물질 중 하나인 PVdF 를 *in situ* crosslinking 기반의 고체

전해질에 첨가하여 고분자의 결정화도를 줄임으로써 이온 전도도를 향상시킴으로써 달성된다. 마지막으로, 제 4 장에서는 이전 장에서 발견된 주요 결과를 요약한다.

종합하자면, 본 학위논문을 통해 고에너지밀도 전지 구현을 위한 새로운 전지 요소 공정 개발시 다양한 방법으로 전도도를 개선할 수 있는 방법을 제공하고자 하며, 이는 향후 차세대 전지 개발에 있어 중요한 통찰력을 제공할 것이다.

주요어: 전도도, 건식 양극, 오존 처리, 탄소나노튜브, 하이브리드 고체 전해질, 결정화도

학번: 2018-34787

List of Publications

International Publications

International Peer-Reviewed Journals (First Author)

1. **H. Kim**†, J. H. Lim†, T. Lee, J. An, H. Kim, H. Song, H. Lee, J. W. Choi*, J. H. Kang*, "Ozone-Treated Carbon Nanotube as a Conductive Agent for Dry-Processed Lithium-Ion Battery Cathode", *ACS Energy Letters*, **2023**, *8*, 3460-3466 (†Co-first author) (IF = 23.991).
2. J. H. Kim†, **H. Kim**†, W.-J. Kim, Y. -C. Kim, J. Y. Jung, D. Y. Rhee, J. H. Song, W. Cho*, M. -S. Park*, "Incorporation of Titanium into Ni-Rich Layered Cathode Materials for Lithium-Ion Batteries", *ACS Applied Materials and Interfaces*, **2020**, *12*, 12204-12211 (†Co-first author) (IF = 10.383).

International Peer-Reviewed Journals (Co-Author)

1. N. Lee, J. Lee, T. Lee, J. Oh, I. Hwang, G. Seo, **H. Kim**, J. W. Choi*, "Rationally Designed Solution-Processible Conductive Carbon Additive Coating for Sulfide-based All-Solid-State Batteries", *ACS Applied Materials & Interfaces*, **2023**, online published (IF = 10.383).
2. J. Lee, S. H. Choi, G. Im, K.-J. Lee, T. Lee, J. Oh, N. Lee, **H. Kim**, Y. Kim, S. Lee, J. W. Choi*, "Room-Temperature Anode-Less All-Solid-State Batteries via the Conversion Reaction of Metal Fluorides", *Advanced*

Materials, **2022**, *34*, 2203580 (IF = 32.086).

3. J. Oh, S. H. Choi, B. Chang, J. Lee, T. Lee, N. Lee, **H. Kim**, Y. Kim, G. Im, S. Lee,* J. W. Choi*, "Elastic Binder for High Performance Sulfide-Based All-Solid-State Batteries", *ACS Energy Letters*, **2022**, *4*, 1374-1382 (IF = 23.991).
4. J. Lee, K. Lee, T. Lee, **H. Kim**, K. Kim, W. Cho, A. Coskun, K. Char*, J. W. Choi*, "In situ Deprotection of Polymeric Binders for Solution-Processible Sulfide-based All-Solid-State Batteries", *Advanced Materials*, **2020**, *32*, 2001702 (IF = 32.086).
5. S. E. Jerng, B. Chang, H. Shin, **H. Kim**, T. Lee, K. Char, J. W. Choi*, "Pyrazine-linked 2D Covalent Organic Frameworks as Coating Material for High-Nickel Layered Oxide Cathodes in Lithium-Ion Batteries", *ACS Applied Materials and Interfaces*, **2020**, *12*, 10597-10606 (IF = 10.383).

Patents

1. 최장욱, 김현태, "리튬이차전지 전극 코팅 방법, 및 이에 따라 제조한 전극을 포함하는 리튬이차전지", 출원번호 10-2018-0002678
2. 최근호, 조용일, 송한나, 김현진, 이현하, 박찬범, 강종헌, 최장욱, 김현태, 임지현, "표면 개질된 탄소나노튜브를 활용한 리튬이차전지용 전극 및 이의 제조방법", 출원번호 10-2022-0178834